

## REVERBERATION MEASUREMENTS OF THE INNER RADIUS OF THE DUST TORUS IN 17 SEYFERT GALAXIES

SHINTARO KOSHIDA<sup>1</sup>, TAKEO MINEZAKI<sup>2</sup>, YUZURU YOSHII<sup>2,3</sup>, YUKIYASU KOBAYASHI<sup>4</sup>, YU SAKATA<sup>2,5</sup>, SHOTA SUGAWARA<sup>2,5</sup>, KEIGO ENYA<sup>6</sup>, MASAHIRO SUGANUMA<sup>4</sup>, HIROYUKI TOMITA<sup>7</sup>, TSUTOMU AOKI<sup>7</sup>, AND BRUCE A. PETERSON<sup>8</sup>

## ABSTRACT

We present the results of a dust reverberation survey for 17 nearby Seyfert 1 galaxies, which provides the largest homogeneous data collection for the radius of the innermost dust torus. A delayed response of the  $K$ -band light curve after the  $V$ -band light curve was found for all targets, and 49 measurements of lag times between the flux variation of the dust emission in the  $K$  band and that of the optical continuum emission in the  $V$  band were obtained by the cross-correlation function analysis and also by an alternative method for estimating the maximum likelihood lag. The lag times strongly correlated with the optical luminosity in the luminosity range of  $M_V = -16$  to  $-22$  mag, and the regression analysis was performed to obtain the correlation  $\log \Delta t$  (days)  $= -2.11 - 0.2M_V$  assuming  $\Delta t \propto L^{0.5}$ , which was theoretically expected. We discuss the possible origins of the intrinsic scatter of the dust lag-luminosity correlation, which was estimated to be approximately 0.13 dex, and we find that the difference of internal extinction and delayed response of changes in lag times to the flux variations could have partly contributed to intrinsic scatter. However, we could not detect any systematic change of the correlation with the subclass of the Seyfert type or the Eddington ratio. Finally, we compare the dust reverberation radius with the near-infrared interferometric radius of the dust torus and the reverberation radius of broad Balmer emission lines. The interferometric radius in the  $K$  band was found to be systematically larger than the dust reverberation radius in the same band by about a factor of two, which could be interpreted by the difference between the flux-weighted radius and the response-weighted radius of the innermost dust torus. The reverberation radius of the broad Balmer emission lines was found to be systematically smaller than the dust reverberation radius by about a factor of 4–5, which strongly supports the unified scheme of the Seyfert type of active galactic nuclei (AGNs). Moreover, we examined the radius-luminosity correlations for the hard X-ray (14–195 keV) and the [O IV] $\lambda$ 25.89  $\mu$ m emission-line luminosities, which would be applicable for obscured AGNs.

*Subject headings:* dust, extinction — galaxies: active — galaxies: Seyfert — infrared: galaxies

## 1. INTRODUCTION

An active galactic nucleus (AGN) is known as one of the most luminous populations in the Universe, and its enormous radiative energy is powered by mass accretion onto the supermassive black hole (SMBH). Many observations have indicated that an optically and geometrically thick torus consisting of gas and dust surrounds the SMBH and accretion disk (e.g., Telesco et al. 1984; Antonucci & Miller 1985; Miller & Goodrich 1990), which could be a gas reservoir

for supplying accreting mass onto the accretion disk (e.g., Krolik & Begelman 1988). This dust torus is regarded as a key structure for the unified scheme of AGNs, which explains differences between type-1 and type-2 AGNs with respect to the viewing angle and obscuration by the dust torus (e.g., Antonucci 1993). In this scheme, type-1 AGNs with broad emission lines (BELs) are classified as type-2 AGNs if the broad emission-line region (BLR) is obscured by the dust torus.

The nature of the dust torus has been extensively investigated by observational and theoretical methods. The near-infrared continuum emission of type-1 AGNs is considered to be dominated by the thermal re-radiation of hot dust driven by the reprocessing of the ultraviolet (UV)–optical continuum emission from the accretion disk (e.g., Rees et al. 1969; Barvainis 1987; Kobayashi et al. 1993; Landt et al. 2011). In addition, significant research has been conducted to explain the infrared spectral energy distribution (SED) of AGNs and to understand the dust torus structure (e.g., Pier & Krolik 1992; Nenkova et al. 2002, 2008; Dullemond & van Bemmelen 2005; Schartmann et al. 2005, 2008; Hönig et al. 2006; Mor et al. 2009; Deo et al. 2011). However, since the apparent size of the dust torus is so compact, it has been almost impossible to resolve and examine the detailed structure of the dust torus directly by imaging observation.

Reverberation mapping observation provides a unique

<sup>1</sup> Center of Astro Engineering and Department of Electrical Engineering, Pontificia Universidad Católica de Chile, Av. Vicuña Mackenna 4868, Chile; skoshida@ing.puc.cl

<sup>2</sup> Institute of Astronomy, School of Science, University of Tokyo, 2-21-1 Osawa, Mitaka, Tokyo 181-0015, Japan; minezaki@ioa.s.u-tokyo.ac.jp

<sup>3</sup> Research Center for the Early Universe, School of Science, University of Tokyo, 7-3-1 Hongo, Bunkyo-ku, Tokyo 113-0013, Japan

<sup>4</sup> National Astronomical Observatory, 2-21-1 Osawa, Mitaka, Tokyo 181-8588, Japan

<sup>5</sup> Department of Astronomy, School of Science, University of Tokyo, 7-3-1 Hongo, Bunkyo-ku, Tokyo 113-0013, Japan

<sup>6</sup> Institute of Space and Astronautical Science, Japan Aerospace Exploration Agency, 3-1-1, Yoshinodai, Sagami-hara, Kanagawa 229-8510, Japan

<sup>7</sup> Kiso Observatory, Institute of Astronomy, School of Science, University of Tokyo, 10762-30 Mitake, Kiso, Nagano 397-0101, Japan

<sup>8</sup> Mount Stromlo Observatory, Research School of Astronomy and Astrophysics, Australian National University, Weston Creek P.O., ACT 2611, Australia

and important tool for investigating the structures of innermost dust tori (Clavel et al. 1989; Baribaud et al. 1992; Glass 1992; Sitko et al. 1993; Oknyanskii 1993; Nelson 1996a; Oknyanskij et al. 1999; Nelson & Malkan 2001; Oknyanskij & Horne 2001; Glass 2004; Lira et al. 2011; Pozo Nuñez et al. 2014). A time lag between the variation of optical flux originating in the accretion disk and that of near-infrared flux in the innermost dust torus can be interpreted as the light-travel time from the accretion disk to the dust torus, which corresponds to the radius of the innermost dust torus. The Multicolor Active Galactic Nuclei Monitoring (MAGNUM) project (Yoshii 2002; Yoshii, Kobayashi, & Minezaki 2003) conducted extensive monitoring observations in optical and near-infrared wavelengths for a number of type-1 AGNs to obtain precise estimates of the radius of the innermost dust torus. Indeed, lag times of weeks to months corresponding to 0.01–0.1 pc were obtained for several Seyfert galaxies from optical and near-infrared monitoring observations, in which a strong correlation between lag time and optical luminosity was found to be consistent with  $\Delta t_{\text{dust}} \propto L^{0.5}$  (Minezaki et al. 2004; Suganuma et al. 2004, 2006; Koshida et al. 2009). Moreover, Suganuma et al. (2006) reported that the dust lag placed an upper boundary on the lag of the BELs, which strongly supports the unified scheme of AGNs.

Recent advancement in infrared interferometry has enabled milliarcsecond-scale measurement of the dust tori for bright AGNs, which has become an important tool for studying the structure of the dust torus. Near-infrared interferometric observations have been applied to less than 10 type-1 AGNs for estimating the radius of the innermost dust torus (Swain et al. 2003; Kishimoto et al. 2009; Pott et al. 2010; Kishimoto et al. 2011; Weigelt et al. 2012). These radii were found to be scaled approximately as  $r_{\text{dust}} \propto L^{0.5}$ , and their values were found to be of the same order as the dust reverberation radii (Kishimoto et al. 2009, 2011).

Such luminosity correlation is expected from a model in which the dust temperature and the inner radius of the dust torus are determined by radiation equilibrium and sublimation of dust, respectively. Barvainis (1987) quantitatively estimated the inner radius of the dust torus by considering the wavelength-dependent absorption efficiency of dust grains, and Kishimoto et al. (2007) expressed dependency on dust grain size as

$$R_{\text{sub}} = 1.3 \left( \frac{L_{\text{UV}}}{10^{46} \text{ erg/s}} \right)^{0.5} \left( \frac{T_{\text{sub}}}{1500 \text{ K}} \right)^{-2.8} \left( \frac{a}{0.05 \mu\text{m}} \right)^{-0.5} \text{ pc}, \quad (1)$$

where  $L_{\text{UV}}$ ,  $T_{\text{sub}}$ , and  $a$  are the UV luminosity of the accretion disk, sublimation temperature of dust, and dust grain size, respectively. Although the previously observed luminosity dependency of the radius of the innermost dust torus is consistent with the theoretical expectation, Kishimoto et al. (2007) found that the innermost torus radii based on dust reverberation were systematically smaller than those based on the theoretical prediction of Equation (1), assuming  $T_{\text{sub}} = 1500 \text{ K}$  and  $a = 0.05 \mu\text{m}$ , by a factor of  $\sim 3$ . They proposed that this discrepancy could be explained by a higher sublimation temperature or a larger grain size, although the for-

mer case would be disfavored by the near-infrared colors of AGNs. On the contrary, Kawaguchi & Mori (2010, 2011) developed a reverberation model for a clumpy dust torus considering the anisotropic illumination of the accretion disk. They presented that dust clouds could survive closer to the accretion disk on the equatorial plane than at the expected sublimation radius by assuming isotropic illumination, which could explain the dust lag discrepancy. They further reported that according to the model, the dust lag increases with the viewing angle of the dust torus, and they suggested that the difference in the viewing angle is primarily responsible for the scatter of the dust lag-luminosity correlation.

In this study, we present 49 measurements of lag time between optical and near-infrared light curves for 17 nearby AGNs obtained by the MAGNUM project, which is the largest collection of systematic survey data of dust reverberation. By estimating the radii of the innermost dust tori from the data, we discuss the structure of AGN dust tori. In Section 2, we describe the target AGNs and the procedures of observation, reduction, and photometry. In addition, we describe the subtraction of contaminated flux by the host-galaxy starlight and narrow emission lines for estimating the optical continuum emission from the accretion disk. In Section 3, we measure the lag time between optical and near-infrared flux variations by using cross-correlation function (CCF) analysis. In Section 4, we examine the lag-luminosity correlation and its scatter on the basis of our uniformly analyzed largest dust reverberation sample. In Section 5, we compare the structure around the BLR and the innermost dust torus determined by our reverberation results with those of near-infrared interferometry and BEL reverberation. In addition, we discuss the secondary dependence of the dust lag on the Seyfert subclass and the mass accretion rate. We summarize the results in Section 6. We assume the cosmology of  $H_0 = 73 \text{ km s}^{-1} \text{ Mpc}^{-1}$ ,  $\Omega_m = 0.27$ , and  $\Omega_\Lambda = 0.73$  according to Spergel et al. (2007) throughout this study.

## 2. OBSERVATIONS AND PHOTOMETRY

We briefly describe the procedures of observation, data reduction, photometry, and estimation of host-galaxy and narrow emission-line fluxes. These procedures follow those presented in previous studies (Suganuma et al. 2006; Koshida et al. 2009; Sakata et al. 2010).

### 2.1. Targets

We focus on 17 type-1 AGNs from the MAGNUM targets that exist in the local Universe with redshifts of less than 0.05. The target AGNs and their basic parameters are listed in Table 1, and their portrait images are presented in Figure 1. Because these nearby Seyfert galaxies are less luminous, their timescales of flux variation are considered to be relatively short, and multiple features such as local peaks and valleys in the light curve enable the precise measurement of the lag times. In addition, their host-galaxy flux can be estimated by surface brightness fitting more reliably than that of distant quasi-stellar objects (QSOs). Of the 17 target AGNs, 14 were selected from the type-1 AGNs for which the BEL lag had been determined by reverberation mapping observations (Wandel et al. 1999; Onken et al. 2003;

Denney et al. 2006); two targets, IRAS 03450+0055 and Mrk 744, were selected from those for which dust reverberation mapping observations had been performed (Nelson 1996a,b); and the last target, MCG +08-11-011, was taken from Enya et al. (2002) for which large amplitudes of flux variation in near-infrared wavebands had been detected. The optical luminosity of the targets ranged from  $M_V = -15.8$  to  $-22.2$  after the host-galaxy flux was subtracted (see Section 2.4).

## 2.2. Observations

Monitoring observations were conducted by using the multicolor imaging photometer (MIP) mounted on the MAGNUM telescope (Kobayashi et al. 1998a,b). The MIP has a field-of-view of  $1.5 \times 1.5$  arcmin<sup>2</sup>; it is capable of simultaneously obtaining images in optical ( $U$ ,  $B$ ,  $V$ ,  $R$ , and  $I$ ) and near-infrared ( $J$ ,  $H$ , and  $K$ ) bands by splitting the incident beam into two different detectors including an SITe CCD ( $1024 \times 1024$  pixels,  $0.277$  arcsec pixel<sup>-1</sup>) and an SBRC InSb array ( $256 \times 256$  pixels,  $0.346$  arcsec pixel<sup>-1</sup>).

Observations were conducted most frequently in the  $V$  and  $K$  bands. The  $V$  band aims to obtain optical continuum emission from the accretion disk, avoiding the contamination of variable BELs such as the Balmer series. On the contrary, the  $K$  band aims to obtain reprocessed thermal emission of hot dust located at the innermost region of the dust torus, in which such thermal emission dominates over the power-law continuum emission from the accretion disk. In this study, we focus on the results derived from the light curves in these bands.

Monitoring observations with the MAGNUM telescope began in 2001–2003, although that for NGC 3516 and NGC 4593 began in 2005. We present the data obtained through 2006–2007 to include monitoring spans of 3–7 years. The typical monitoring intervals were configured to be shorter for less luminous targets for which shorter lag times were expected, and they were from a few days to 20 days. The observational parameters are listed in Table 2.

## 2.3. Reduction and Photometry

The images were reduced using IRAF<sup>9</sup>. We followed the standard procedures for image reduction such as bias or sky subtraction and flat fielding, with small corrections applied for non-linear detector response.

As shown in Figure 1, the MIP’s limited field-of-view prevented us from obtaining suitable stars for the reference of the point-spread function (PSF) shape and photometry in the same images as those of bright and extended targets. Therefore, we observed the target AGN and its reference stars alternately to measure the nuclear flux of the target with respect to these reference stars, and aperture photometry with a circular aperture of  $\phi = 8''.3$  in diameter with a sky reference area of a  $\phi = 11''.1 - 13''.9$  annulus was applied instead of difference imaging photometries<sup>10</sup>. Although a relatively

large aperture was selected to keep the photometry stable against the seeing variation, the photometric error of the nuclear flux relative to the reference stars was typically  $0.01$  mag. The fluxes of the reference stars were calibrated with respect to photometric standard stars designated by Landolt (1992) and Hunt et al. (1998) for the  $V$  and  $K$  bands, respectively, and the errors in flux calibration were typically less than  $0.01$  mag. The positions and magnitudes of the reference stars are listed in Table 3. The resultant light curves of the 17 target AGNs in the  $V$  and  $K$  bands are presented in Figures 2–4, and their data are listed in Table 4.

## 2.4. Subtraction of Host-Galaxy Flux

The flux obtained by aperture photometry contained a significant contribution of host-galaxy starlight and thus was subtracted. Nine of the 17 target AGNs are common to those of Sakata et al. (2010), who estimated the host-galaxy fluxes in the optical  $B$ ,  $V$ , and  $I$  bands within the same photometric aperture by surface brightness fitting to the high-resolution *Hubble Space Telescope* (*HST*) Advanced Camera for Surveys images as well as those obtained by MAGNUM. We adopted the same  $V$ -band fluxes of host galaxies reported by Sakata et al. (2010) for these targets. In addition, we adopted the results by Suganuma et al. (2006), who estimated the host-galaxy flux of NGC 7469 in the  $V$  band within the same photometric aperture.

For the remaining seven target AGNs, we estimated the host-galaxy flux in the  $V$  band by surface brightness fitting in the same manner as that reported by Suganuma et al. (2006). We first selected the data obtained at night with good and stable seeing conditions, typically with a PSF full-width at half-maximum of less than  $1.5$  arcsec. All target AGN and reference-star images obtained during the same night were then combined into one image. The target AGN image was fitted by the GALFIT two-dimensional image decomposition program (Peng et al. 2002) with analytic functions for the galaxy component of bulge (de Vaucouleurs’  $R^{1/4}$  profile) and disk (exponential profile), plus a PSF for the AGN nucleus, using the images of the reference stars simultaneously observed as the PSF reference. Finally, aperture photometry was applied to the nucleus-free image created by subtracting the best-fit PSF component from the original image. We adopted the average and scatter of the aperture fluxes of the nucleus-free images over the data obtained during various nights as the host-galaxy flux and its error.

For the host-galaxy fluxes in the  $K$  band, we adopted the results of Minezaki et al. (2004) for NGC4151; those of Suganuma et al. (2006) for NGC 5548, NGC 4051, NGC 3227, and NGC 7469; those of Tomita et al. (2006) for MCG +08-11-011; and those of Tomita (2005) for IRAS 03450+0055, Akn 120. For the remaining 9 target AGNs, we estimated the host-galaxy flux in the  $K$  band by surface brightness fitting in the same manner as that conducted for the  $V$  band. The host-galaxy fluxes within the aperture and their errors are listed in Table 5.

reference star image are slightly different because they were not simultaneously obtained, which makes it difficult to employ difference imaging photometries.

<sup>9</sup> IRAF is distributed by the National Optical Astronomy Observatories, which are operated by the Association of Universities for Research in Astronomy, Inc., under cooperative agreement with the National Science Foundation.

<sup>10</sup> We also note that the PSFs of the target image and the

### 2.5. Subtraction of Narrow Emission-Line Flux

In addition to subtracting the contaminated flux of host-galaxy starlight, we subtracted the contribution of the two strong narrow emission lines, [O III] $\lambda$ 4959 and  $\lambda$ 5007, from the  $V$ -band flux for estimating the flux of the optical continuum emission from the accretion disk. Sakata et al. (2010) estimated the contribution of the narrow emission lines in the  $V$  band; therefore, we adopted their estimates for the nine common targets.

For the remaining eight target AGNs, we estimated the contribution of the narrow emission lines in the  $V$  band in the same manner as that conducted by Sakata et al. (2010). The flux of [O III] $\lambda$ 5007 was compiled from previous research (Boroson & Meyers 1992; Whittle 1992; Kaspi et al. 1996; Marziani et al. 2003; Schmitt et al. 2003; Kaspi et al. 2005), and the flux of [O III] $\lambda$ 4959 was calculated by assuming a theoretical line ratio of [O III] $\lambda$ 5007/[O III] $\lambda$ 4959 = 3.01 (Storey & Zeppen 2000). We then estimated their flux contributions by convolving a narrow-line spectrum with the transmission curve of the  $V$ -band filter. Following Sakata et al. (2010), we adopted 10% of the flux of the narrow-line component as its error. Contributions of the narrow emission lines are also listed in Table 5.

## 3. DUST REVERBERATION ANALYSIS

As presented in Figures 2–4, all targets showed significant flux variations in both bands and delayed responses of the  $K$ -band light curve after that of the  $V$  band, which indicate that the reprocessed thermal radiation of hot dust dominated in the  $K$ -band flux.

In this section, we estimate the lag time between the  $V$ - and  $K$ -band light curves, which corresponds to the radius of the innermost dust torus, by using CCF analysis (White & Peterson 1994; Peterson 2001) as well as by an alternative method for estimating the maximum likelihood lag that was recently developed by Zu, Kochanek, & Peterson (2011). Following the method of Koshida et al. (2009), we first subtracted the accretion-disk component of flux in the  $K$  band to derive the dust torus component, then we applied the CCF analysis and the alternative method to the  $V$ -band light curve and that of the dust torus component in the  $K$  band. In this study, we summarize only the procedures; details for the subtraction of the accretion-disk component and the CCF analysis have been reported in previous studies (Suganuma et al. 2006; Koshida et al. 2009), and those for the alternative method are described in Zu et al. (2011).

### 3.1. Subtraction of the Accretion-Disk Component from the $K$ -Band Flux

Although the thermal radiation of the dust torus usually dominates in the  $K$ -band flux of type-1 AGNs, it contains emission from the accretion disk (Tomita et al. 2006; Kishimoto et al. 2008; Lira et al. 2011). While the host-galaxy flux has no influence on CCF analysis because it is not variable, the superimposed flux variation by the accretion-disk component in the  $K$ -band flux would make the lag time obtained by CCF analysis shorter than the actual lag of the dust-torus emission. Such a result occurs, because the power-law continuum emission from the accretion disk in the near-infrared spectra varies with time and is nearly synchronous with

that in the optical (Tomita et al. 2006; Minezaki et al. 2006; Lira et al. 2011).

Therefore, we estimated the contribution of the accretion disk in the  $K$ -band flux at a certain epoch,  $f_{K,\text{disk}}(t)$ , and subtracted it from the observed  $K$ -band flux prior to CCF analysis. In this study,  $f_{K,\text{disk}}(t)$  was estimated from the  $V$ -band flux by assuming a power-law spectrum of the accretion-disk emission as

$$f_{K,\text{disk}}(t) = f_V(t) \left( \frac{\nu_K}{\nu_V} \right)^{\alpha_\nu}, \quad (2)$$

where  $f_V(t)$  is the  $V$ -band flux at the same epoch after the host-galaxy and narrow emission-line fluxes were subtracted;  $\nu_K$  and  $\nu_V$  are effective frequencies of the  $K$  and  $V$  bands, respectively; and  $\alpha_\nu$  is the power-law index. If no optical photometric data were available at the same epoch,  $f_V(t)$  was obtained by the linear interpolation of the photometric data observed at the closest epochs. Prior to the estimation and subsequent subtraction of the accretion-disk component,  $f_{K,\text{disk}}$ , the observed  $V$ - and  $K$ -band fluxes were corrected for the Galactic extinction according to the NASA/IPAC Extragalactic Database (NED; based on Schlegel et al. 1998).

The spectral shape of the flux variation of accretion-disk emission in optical and near-infrared wavelengths has not been well established. Tomita et al. (2006) applied the multiple regression analysis to the flux variations observed in optical and near-infrared wavebands of a Seyfert galaxy MCG +08–11–011 to estimate the power-law index of the accretion-disk component of the flux variation in optical and near-infrared spectra as  $\alpha_\nu \sim -0.1$  to  $+0.4$ . From the same analysis applied to a number of nearby Seyfert galaxies by Tomita (2005), the value could be estimated as  $\alpha_\nu = +0.10 \pm 0.11$ . According to the standard accretion model (Shakura & Sunyaev 1973), the power-law index  $\alpha_\nu$  increases with wavelength and converges asymptotically on  $\alpha_\nu = +1/3$  in the limit of long wavelength, and the power-law index of the flux variation would be the same in the long-wavelength limit when the standard accretion model is retained during flux variations. Wilhite et al. (2005) derived the composite differential spectrum of QSOs observed by the Sloan Digital Sky Survey and found that it could be fitted well by the power-law form of  $\alpha_\nu = 0$ , although the wavelength range was UV to optical. Kishimoto et al. (2008) conducted spectropolarimetry for radio-loud and -quiet QSOs and obtained  $\alpha_\nu = 0.44 \pm 0.11$ , although the observation was single epoch. From these considerations, we calculated  $f_{K,\text{disk}}$  assuming both  $\alpha_\nu = 0$  and  $+1/3$  to examine a systematic difference in the dust lag estimation.

### 3.2. Measuring the Dust Lag by the CCF Analysis

After subtracting the accretion-disk component from the  $K$ -band flux, we measured the lag time between the flux variation of the thermal emission from the dust torus in the  $K$  band and that of the optical continuum emission from the accretion disk in the  $V$  band. First, we applied widely used, conventional CCF methods that have been employed (White & Peterson 1994; Peterson 2001; Rafter et al. 2011; Barth et al. 2011a,b; Doroshenko et al. 2012; Edri et al. 2012; Grier et al. 2012a; Du et al. 2014).

For comparison with our new results, the bi-directional interpolation (BI) method was adopted, which is the same method as that used in our previous studies (Suganuma et al. 2006; Koshida et al. 2009). The BI method is used to calculate the CCF of the light curves with irregular sampling obtained by monitoring observations, and it incorporates interpolation errors caused by the target's flux variation, as is described subsequently.

With an arbitrary shift of time between the light curves in two different bands,  $\tau$ , we generated the data pairs of fluxes whereby the flux in one band was obtained by actual observation and that in the other band was estimated by the linear interpolation of the light curve. Once the data pairs were produced for all observed data of both bands, a cross correlation for  $\tau$  was calculated by using the set of data pairs. The CCF could then be calculated for any  $\tau$ . Finally, the lag time was determined as the centroid around the peak of the CCF,  $\tau_{\text{cent}}$ , which was calculated by utilizing a part of the CCF near the peak with a value larger than 0.8 times the peak value of the CCF.

The uncertainty of the lag time was estimated by Monte Carlo simulation (Maoz & Netzer 1989). A pair of artificial light curves was generated for the  $V$  and  $K$  bands, and the CCF was calculated to determine the centroid lag,  $\tau_{\text{cent}}$ . The cross-correlation centroid distribution (CCCD) was then derived from a large number of realizations of the simulation, and the uncertainty of the lag time was determined from the CCCD.

Artificial light curves were calculated by the flux randomization (FR) method (Peterson et al. 1998) combined with a method based on the structure function (SF), which simulates the flux variability between the observed data points (Suganuma et al. 2006). According to Gaussian distributions with standard deviations given by the flux-measurement errors for respective data points, the FR method randomly modifies the observed fluxes in each realization. The basic concept of simulating the flux uncertainty at interpolated data points caused by the variability in using SF is described in the following equation. Here, we define SF as

$$SF(\tau) = \left( \frac{1}{N(\tau)} \right) \sum_{i < j} [f(t_i) - f(t_j)]^2 - 2\sigma^2 \quad (3)$$

where  $f(t)$  is the flux at epoch  $t$ ,  $\sigma$  is the average of the observed flux errors of the pair, and  $N(\tau)$  is the number of data pairs; the sum is given by the overall pairs for which  $t_i - t_j = \tau$ . According to this definition,  $(SF(\tau))^{1/2}$  can be interpreted as the standard deviation of flux variation between two observational epochs with a time interval of  $\tau$ . Then, an artificial flux for an arbitrary epoch apart from actual observational epochs can be stochastically realized according to the Gaussian distribution, in which the standard deviation is given by  $(SF(\tau))^{1/2}$ . A detailed procedure for calculating the artificial light curve has been reported by Suganuma et al. (2006).

In Figure 5, the  $V$ -band SF for NGC 4151 is presented as an example of the SF. The power-law form of  $SF(\tau) = \alpha\tau^\beta$  was fitted in the range of the time interval between two times the median of the observational intervals and 0.3 times the entire observation span, in which SF is

considered to be significant (Collier & Peterson 2001). The regression line of the power-law fitting for NGC 4151 is also presented in Figure 5, and the parameters of the power-law fitting of the SFs for all the 17 targets are listed in Table 6. Because the  $K$ -band light curves were smooth and appeared to be well sampled, we applied the SF method described above only for the  $V$ -band data (Koshida et al. 2009).

We conducted 1000 realizations of the Monte Carlo simulation for each target to obtain the CCCD. Realizations were omitted if the significance of the correlation coefficient at the CCF peak was less than 0.90 or if the CCF showed a plateau or multiple peaks. Finally, the lag time of the flux variation of the dust-torus emission in the  $K$  band after that of the emission from the accretion disk,  $\Delta t_K$ , was estimated by a median of the CCCD, and its uncertainty was estimated by 34.1 percentiles in the upper and lower sides of the median of the CCCD.

As shown in Figures 2–4, multiple features in the light curves such as local peaks and valleys were apparent in several AGNs; we estimated their lag times at different epochs. We separated the entire monitoring period into several sections, each of which contained a small number of features of flux variation and more than 30 data pairs for sufficient calculation of significant CCFs. In Figures 6 and 7, CCFs and CCCDs for the individual light curve sections are presented for NGC 4151 as examples. As a result, 49 data of  $\Delta t_K$  were obtained for the 17 target AGNs. The lag times and their errors for all measurements, in addition to the weighted averages of the lag times at different epochs for the individual targets, are listed in Table 7.

To compare the lag times  $\Delta t_K$ , assuming  $\alpha_\nu = 0$  and  $+1/3$  for subtracting the accretion-disk component in the  $K$ -band flux, we plotted all 49 measurements of  $\Delta t_K$  in Figure 8. The lag times  $\Delta t_K$  in which  $\alpha_\nu = 0$  was assumed and those in which  $\alpha_\nu = +1/3$  was assumed strongly correlated, and the best fit linear regression for Figure 8 was  $\log \Delta t_K(\alpha_\nu = +1/3) - \log \Delta t_K(\alpha_\nu = 0) = -0.023 \pm 0.005$ . Therefore, the maximum systematic error for  $\Delta t_K$  caused by the uncertainty of the spectral shape of the flux variation of accretion-disk emission in optical and near-infrared spectra for the subtraction of the accretion-disk component in the  $K$ -band fluxes can be estimated as approximately 5%.

### 3.3. Measuring the Dust Lag by JAVELIN

Next, we applied an alternative method for measuring lag times developed by Zu et al. (2011), the JAVELIN software (formerly known as SPEAR), which is employed in recent reverberation studies (Grier et al. 2012a,b; Dietrich et al. 2012; Grier et al. 2013; Zhang 2013a,b; Shapovalova et al. 2013). Its formalism was originally developed by Rybicki & Kleyana (1994) based on the studies of Press et al. (1992) and Rybicki & Press (1992), and has the advantage that the uncertainties in the interpolation of the light curve data and thus the statistical confidence limits on the lag time including them can be self-consistently estimated under a statistical model of variability.

JAVELIN adopts a damped random walk (DRW) model for flux variation of the UV-optical continuum emission, which has been demonstrated to be a good statistical model for AGN variability (e.g., Kelly et al.

2009; Kozłowski et al. 2010; MacLeod et al. 2010, 2012; Zu et al. 2013), and also assumes a top hat transfer function in the transfer equation of reverberation mapping. Then, it fits the continuum and response light curves using the Markov chain Monte Carlo (MCMC) method to obtain the likelihood distribution for the lag time as well as those for the two DRW model parameters for the continuum variability, the width of the transfer function, and the scaling coefficient that determines the response for a given change in the continuum.

The parameter values of the DRW model and their uncertainties are supplied to the lag-time fitting process as prior distributions, thus they are usually obtained from the continuum light curve before the lag-time fitting. In this study, we obtain lag times for separated monitoring sections, and each of them has less observational data points than those for the entire monitoring period. Therefore, we first obtained the best-fit values of the DRW model parameters from the entire  $V$ -band light curve of each target, then we supplied those best-fit values with very small uncertainties to the lag-time fitting process as prior distributions, thus the DRW model parameters were effectively fixed to those values during the lag-time fitting process. This is a similar way to the SF parameters and the CCCD analysis as described in the previous subsection.

The resultant lag times  $\Delta t_K$  obtained by JAVELIN are also listed in Table 7. In most cases, a single and unambiguous peak of the likelihood distribution for  $\Delta t_K$  could be found. However, the likelihood distribution was sometimes not stable depending on the MCMC control parameters. Additionally, ambiguous multiple peaks sometimes appeared in the likelihood distribution, some of which might be regarded as a single but broad peak in the CCCD. As Zu et al. (2011) reported on an aliasing problem of JAVELIN, it tends to map the  $K$ -band light-curve data into the sampling gaps of the  $V$ -band light curve to decrease the data overlap, then poor light curve sampling would lead to those problems in the lag-time analysis.

In Figure 9, we plotted all 49 measurements of  $\Delta t_K$  based on the two different methods and found that the lag time obtained by JAVELIN is generally in accordance with that obtained by the CCF analysis, although the scatter of the data points around the best fit regression is larger than that expected from their estimated errors. The best fit linear regressions for them are  $\log \Delta t_K(\text{CCF}) - \log \Delta t_K(\text{JAVELIN}) = -0.041 \pm 0.017$  with an additional scatter of  $\sigma_{\Delta t} = 0.072$  dex in both directions for the reduced  $\chi^2$  to achieve unity, and  $-0.049 \pm 0.016$  with  $\sigma_{\Delta t} = 0.067$  dex for  $\alpha_\nu = 0$  and  $+1/3$ , respectively. Therefore, the systematic difference for  $\Delta t_K$  between the two different lag analysis methods can be estimated as approximately 10%. In addition, as will be presented in the next section, the scatter around the dust lag-luminosity correlation for  $\Delta t_K(\text{JAVELIN})$  is as much as that for  $\Delta t_K(\text{CCF})$ . By these considerations, we use the  $\Delta t_K$  data obtained by using JAVELIN as well as those obtained by using the CCF analysis in the subsequent discussions, although the data plots are represented by  $\Delta t_K(\text{CCF}; \alpha_\nu = 0)$  for clarity.

#### 4. LAG-LUMINOSITY CORRELATION FOR THE DUST TORUS

We present 49 measurements of dust reverberation for the 17 type-1 AGNs, the data for which were analyzed carefully and uniformly to obtain precise estimates of lag times. This sample is the largest homogeneous collection of dust reverberation and observations for the size of the inner dust torus. By using these results, we examined the correlation between the dust lag and optical luminosity, which has been reported in previous studies (Suganuma et al. 2006; Kishimoto et al. 2011). In the subsequent sections, the lag times were corrected for time dilation according to the object redshift, the maximum of which was approximately 5%.

##### 4.1. Estimation of the Optical Luminosities of an AGN

We first calculated an “average”  $V$ -band flux,  $\bar{f}_V$ , for each corresponding period in which the  $\Delta t_K$  was obtained, following Koshida et al. (2009). Rather than obtaining a simple average of the observed fluxes, which could be biased by unequal intervals of observation, an average flux from the interpolated  $V$ -band light curve with equal intervals generated in the process of the CCF analysis was calculated as a measure of  $\bar{f}_V$ . We obtained the distribution of the average  $V$ -band flux from all realizations of the Monte Carlo simulation, and  $\bar{f}_V$  and its error were estimated by a centroid and 34.1 percentiles in both sides of the distribution. In Figures 6 and 7, the distributions of the average  $V$ -band flux for respective epochs are presented for NGC 4151 as an example.

The absolute magnitude in the  $V$  band,  $M_V$ , was then calculated from  $\bar{f}_V$  and the recession velocity of the target, assuming the cosmological parameters. The recession velocity was obtained from the local flow corrected velocity of the Virgo infall + Great Attractor + Shapley supercluster displayed by the NED, which was originally based on Mould et al. (2000). The  $V$ -band absolute magnitude  $M_V$  and their errors of the targets for all epochs of lag-time measurements, in addition to the weighted averaged  $M_V$  for the individual targets, are listed in Table 7. The error of  $M_V$  was estimated from a root sum square of the errors of  $\bar{f}_V$ , host-galaxy flux, narrow emission-line flux, and flux calibration caused by uncertainty of the reference star magnitudes.

##### 4.2. Correlation between the Dust Lag and Optical Luminosity

In Figure 10, the dust lags  $\Delta t_K$  of the target AGNs were plotted against their  $V$ -band absolute magnitudes  $M_V$ . A clear correlation between  $\Delta t_K$  and  $M_V$  over an absolute magnitude range of  $M_V \approx -16$  to  $-22$  was detected for the 49 measurements of dust lags and the weighted averaged lags for the 17 individual target AGNs, represented in the figure by open and filled circles, respectively. This correlation has been presented in previous studies for a smaller sample (Oknyanskij & Horne 2001; Minezaki et al. 2004; Suganuma et al. 2006).

To examine the correlation between the dust lag and optical luminosity, a regression analysis was applied with a linear equation in the form of

$$\log \Delta t_K = a + b M_V. \quad (4)$$

This regression analysis was applied to the data assuming  $\alpha_\nu = 0$  and  $+1/3$  for both  $\Delta t_K(\text{JAVELIN})$  and  $\Delta t_K(\text{CCF})$ . We assumed the slope of the regression line

as  $b = -0.2$ , following Minezaki et al. (2004), because the slope is expected from the simple model of the dust sublimation radius, as presented in Equation (1). In addition, Kishimoto et al. (2011) reported that such correlation is consistent with the slope for the data combined with the dust reverberation and near-infrared interferometry, including AGNs with higher luminosity. The regression was calculated by the generalized multivariate least-squares method presented by Jefferys (1980), weighted by the errors of  $\Delta t_K$  and  $M_V$ . A detailed discussion on the slope of the correlation will be available in a forthcoming paper based on the systematic measurements of dust reverberation with the data for AGNs with higher luminosity.

We first fit the model to the data of the 49 measurements of dust lags and to those of the weighted averaged lags for the 17 targets; the results are listed in Table 8. The derived parameters agreed well; however, the reduced  $\chi^2$  of the fitting was significantly larger than unity. That is, the fitting residuals were much larger than those expected from the measurement errors of  $\Delta t_K$  and  $M_V$ .

Peculiar velocity was a source of error for our estimation of  $M_V$ , whereby the effect was larger for closer objects. Since the values presented for the peculiar velocity dispersion,  $\sigma_{\text{pec}}^2$ , differ slightly (e.g., Watkins 1997; Gibbons et al. 2001; Radburn-Smith et al. 2004; Masters et al. 2006), we assumed  $\sigma_{\text{pec}} = 200 \text{ km s}^{-1}$  and  $300 \text{ km s}^{-1}$  to estimate the uncertainty of  $M_V$  caused by peculiar velocity. Then, incorporating this  $M_V$  error by root-sum-square, we fit the model to the data of the weighted averaged lags for the 17 targets. These results are also listed in Table 8. The reduced  $\chi^2$  of the fitting decreased considerably when the peculiar velocity dispersion was incorporated; however, it remained much larger than unity. Therefore, significant intrinsic scatter was expected to reside in the dust lag-luminosity correlation.

We then fitted the model to the data of the weighted averaged lags for the 17 targets, adding an error  $\sigma_{\text{add}}$  to the error of  $\log \Delta t_K$  data by root-sum-square for the reduced  $\chi^2$  to achieve unity. The fitting was also applied to the data incorporating the peculiar velocity dispersion; the fitting results as well as  $\sigma_{\text{add}}$  are listed in Table 8. The derived parameters  $a$  and  $\sigma_{\text{add}}$  agreed well among them, and we adopted  $a = -2.12 \pm 0.04$  with  $\sigma_{\text{add}} = 0.14 \text{ dex}$  ( $\alpha_\nu = 0$  assumed) and  $a = -2.15 \pm 0.04$  with  $\sigma_{\text{add}} = 0.14 \text{ dex}$  ( $\alpha_\nu = +1/3$  assumed) for  $\Delta t_K(\text{CCF})$ , and  $a = -2.08 \pm 0.04$  with  $\sigma_{\text{add}} = 0.16 \text{ dex}$  ( $\alpha_\nu = 0$  assumed) and  $a = -2.10 \pm 0.04$  with  $\sigma_{\text{add}} = 0.16 \text{ dex}$  ( $\alpha_\nu = +1/3$  assumed) for  $\Delta t_K(\text{JAVELIN})$ , from the fittings incorporating the peculiar velocity dispersion. The best-fit regression lines are also presented in Figure 10. The systematic difference between two linear regressions between the data assuming  $\alpha_\nu = 0$  and  $+1/3$  was  $0.02 - 0.03 \text{ dex}$ , and that between the CCF analysis and JAVELIN was  $0.04 - 0.05 \text{ dex}$ . We adopted  $\alpha_\nu = +0.10$  (Tomita 2005) tentatively for the spectral shape of the flux variation of accretion-disk emission in optical and near-infrared spectra for the subtraction of the accretion disk, and we estimated  $a = -2.13 \pm 0.04$  for  $\Delta t_K(\text{CCF})$  and  $a = -2.09 \pm 0.04$  for  $\Delta t_K(\text{JAVELIN})$ . Then, we adopt  $a = -2.11 \pm 0.04$  for the parameter of the dust lag-luminosity correlation in Equation (4). The parameter of  $a = -2.11 \pm 0.04$  was consis-

tent with that presented in a previous study ( $a = -2.15$ ; Minezaki et al. 2004). In addition, regarding the scatter  $\sigma_{\Delta t}$  between  $\Delta t_K(\text{CCF})$  and  $\Delta t_K(\text{JAVELIN})$  as the systematic scatter associated with the lag-analysis methods,  $\sigma_{\text{int}} = \sqrt{\sigma_{\text{add}}^2 - \sigma_{\Delta t}^2} \approx 0.13 \text{ dex}$  can be interpreted as intrinsic scatter in the dust lag-luminosity correlation.

#### 4.3. Possible Origin of Intrinsic Scatter in the Dust Lag-Luminosity Correlation

Although the central engine of the type-1 AGN is not considered to be as heavily obscured by the dust torus as that of the type-2 AGN, a small but different amount of extinction could exist in type-1 AGNs to create a possible source of scatter in the dust lag-luminosity correlation. Cackett et al. (2007) estimated the intrinsic color excess of 14 AGNs by the flux variation gradient (FVG) method (Winkler et al. 1992) and the Balmer decrement method. The estimates obtained from both methods were consistent; therefore, the difference between the estimates by the two methods could be regarded as the sum of the intrinsic uncertainties of the methods themselves. We estimated the standard deviation of the uncertainty of the FVG method as  $0.041 \text{ mag}$ . In fact, of the 14 target AGNs of Cackett et al. (2007), 11 AGNs are in common with our targets. For these targets, the standard deviation of color excess obtained by the FVG method was estimated as  $\sigma_{E(B-V),\text{FVG}} = 0.076 \text{ mag}$ , and the intrinsic standard deviation of color excess was estimated as  $\sigma_{E(B-V)} = 0.064 \text{ mag}$ . Assuming  $A_V/E(B-V) = 3.1$ , this value corresponds to the scatter of approximately  $0.2 \text{ mag}$  in  $M_V$  or  $0.04 \text{ dex}$  in  $\log \Delta t_K$ , which is insufficient for explaining the scatter of  $\sigma_{\text{int}} \approx 0.13 \text{ dex}$  in the correlation.

The difference in the spectral shape of the flux variation of accretion-disk emission between targets, which would be caused by a different amount of intrinsic extinction or by other reasons, would contribute the scatter in the dust lag-luminosity correlation. For example, the intrinsic standard deviation of  $\sigma_{\alpha_\nu} = 0.1$ , which could be caused by the intrinsic standard deviation of color excess of  $\sigma_{E(B-V)} = 0.054 \text{ mag}$ , would originate the scatter of approximately  $0.01 \text{ dex}$  in  $\log \Delta t_K$ . This result is also insufficient for explaining the scatter of  $\sigma_{\text{int}} \approx 0.13 \text{ dex}$  in the correlation.

We then focused on the changes in dust torus size with the flux variation as an additional possible source of scatter in the dust lag-luminosity correlation. Koshida et al. (2009) found that although the dust lag changed with the flux variation in the  $V$  band, the dust lags at different epochs did not follow the relation of  $\Delta t \propto L_V^{0.5}$  for NGC 4151. They suggested that the destruction and formation of the dusty clouds composing the dust torus would not respond instantaneously with the variation of incident flux. In addition, Pott et al. (2010) and Kishimoto et al. (2011) did not detect the size change of the inner dust torus during the flux variation in the multi-epoch near-infrared interferometric data for the same object, and at last Kishimoto et al. (2013) found its size change from the longer term monitoring observation by the near-infrared interferometry, which did not follow the relation of  $\Delta t \propto L_V^{0.5}$  as well. Indeed, as shown in Figure 10, the multi-epoch data of  $\Delta t_K$  and  $M_V$  for a target AGN appeared to scatter around

the global dust lag-luminosity correlation. This behavior of the dust torus size would broaden the correlation unless the dust lag and luminosity for an object were time-averaged over a long span. The scatter was then estimated from the multi-epoch data for the 11 target AGNs. The median of the standard deviations of distance from the  $\Delta t_K \propto L_V^{0.5}$  correlation for respective targets was 0.11 dex, which is significant but still has some room to account for the  $\sigma_{\text{int}} \approx 0.13$  dex scatter.

Even after these possible contributions to the scatter were subtracted, an intrinsic scatter of  $\sigma \lesssim 0.1$  dex in  $\log \Delta t_K$  was expected to remain in the dust lag-luminosity correlation and would be produced by diversities of characteristics in type-1 AGNs such as the viewing angle of the accretion disk and dust torus or by the Eddington ratio of the mass accretion rate. The dependency of dust lag on these parameters is discussed in Section 5.

## 5. DISCUSSION

### 5.1. Change in Dust Lag with Viewing Angle and Mass Accretion Rate

The dust reverberation models predicted that the transfer function, a response of flux variation of the dust emission on an impulse of the UV-optical continuum emission, would change with the viewing angle of the dust torus (Barvainis 1992; Kawaguchi & Mori 2011). In particular, Kawaguchi & Mori (2011) reported that the centroid of the transfer function, which should be interpreted as the lag between flux variations, increases with the viewing angle according to the reverberation model with a clumpy torus, because the self-occultation and waning effects selectively decrease the emission from dusty clouds with a shorter lag at the side in closest proximity to the observer.

We then examined a possible systematic change in dust lag with the viewing angle. In Figure 11, we plotted the residuals of the dust lag from the best-fit regression line (for the data assuming  $\alpha_\nu = 0$ ) against the subclass of the Seyfert type as an indicator of viewing angle. The subclasses of intermediate Seyfert galaxies (S1.0, S1.2, S1.5, and S1.8) for the 14 target AGNs were obtained from Véron-Cetty & Véron (2010). Among them, Mrk 335 and NGC 4051 were classified as narrow-line Seyfert 1 (S1n) by Véron-Cetty & Véron (2010), and a subclass of S1.0 was assigned following Osterbrock & Martel (1993). The error of the residual was estimated from those of the lag time and  $M_V$ .

As shown in Figure 11, we did not detect systematic changes of dust lag with the subclass of the Seyfert type, although Kawaguchi & Mori (2011) estimated that the dust lag systematically shifted approximately 0.4 dex with a change of  $0^\circ - 45^\circ$  in the viewing angle. However, a possible correlation between the dust lag and viewing angle could not be ruled out, because a certain amount of scatter in the relationship between the Seyfert type and viewing angle was expected from a realistic clumpy dust torus model, which consists of dusty clouds stochastically distributed following the probability distribution as a function of the angle from the equatorial plane (Elitzur 2012). A better estimate of the viewing angle is required for further investigation.

Next, we focused on the Eddington ratio, which is the mass accretion rate relative to the mass of the central

black hole. When the mass accretion rate exceeds the Eddington rate, a slim disk that is optically and geometrically thick appears (Abramowicz et al. 1988). Its disk illumination toward the dust torus located on the equatorial plane would be suppressed by disk self-occultation (Kawaguchi & Mori 2011; Kawakatu & Ohsuga 2011); therefore, we can expect that the inner radius of the dust torus decreases as the mass accretion rate increases according to the stronger anisotropy of disk illumination. However, Kawaguchi & Mori (2011) reported that according to their reverberation model, the change in dust lag would not be as significant as the mass accretion rate.

In Figure 12, we plotted the residuals of the dust lag from the best-fit regression line (for the data assuming  $\alpha_\nu = 0$ ) against the Eddington ratio,  $L_{\text{bol}}/L_{\text{Edd}}$ , for the 13 target AGNs with black-hole masses measured by BLR reverberation mapping (Peterson et al. 2004; Bentz et al. 2006a, 2007; Denney et al. 2010; Grier et al. 2012b). NGC 4593 was omitted because of its large error in black-hole mass. The bolometric luminosity was estimated from the luminosity of the optical continuum emission as  $L_{\text{bol}} = 9 \times \lambda L_\lambda(5100\text{\AA})$  (Kaspi et al. 2000), where  $L_\lambda(5100\text{\AA})$  was calculated from  $L_V$  by assuming a power-law spectrum of  $f_\nu \propto \nu^0$ . The error of the Eddington ratio was estimated from those of  $M_V$  and black-hole mass.

As shown in Figure 12, we did not detect systematic changes in dust lag with the Eddington ratio. In fact, the Eddington ratios of all 13 targets were smaller than  $\sim 0.1$  and were believed to be too small for slim disk formation. Because a standard accretion disk with a small mass accretion rate would not change the illumination anisotropy as much as the mass accretion rate (Kawaguchi & Mori 2011), the absence of a systematic trend of dust lag with the Eddington ratio in Figure 12 is consistent with the model. The observation of an AGN with a super-Eddington mass accretion rate is required to investigate the effect of anisotropic illumination of the slim disk.

### 5.2. Structure of the BLR and Inner Dust Torus

Reverberation observations for BELs and dust thermal emission provide an important tool for investigating the structure of the BLR and innermost dust torus. Suganuma et al. (2006) compared the results of the dust reverberation with those for BELs and demonstrated that the innermost dust torus was located just outside of the BLR. Infrared interferometry is also an important tool for investigating the dust torus. Kishimoto et al. (2011) reported that the radius of the innermost dust torus obtained by near-infrared interferometry was consistent with the dust reverberation radius; however, the former tended to be roughly equal to or slightly larger than the latter. On the basis of our new results of the largest homogeneous sample of dust reverberation, we discuss in this section the structure of the BLR and the innermost dust torus.

In Figure 13, we plotted the radii of the innermost dust torus obtained by reverberation and near-infrared interferometry, as well as the reverberation radius of the BLR, against the optical V-band luminosity. The dust reverberation radii and optical luminosities were obtained from our results, and those of the near-infrared



interferometry were obtained from the data compiled by Kishimoto et al. (2011) and Weigelt et al. (2012). The lag-luminosity correlation of BLR has been investigated by many authors. Among the data presented in such studies, we used that obtained by the reverberation observation of Balmer emission lines (mostly  $H\beta$ ) compiled by Bentz et al. (2009a), because they presented an accurate estimation of the optical luminosity by using the *HST* images to carefully subtract the host-galaxy flux.

In Figure 14, the radii of the innermost dust torus and BLR ( $H\beta$ ) were plotted against the hard X-ray (14–195 keV) luminosity, and in Figure 15, they were plotted against the luminosity of  $[O\ IV]\lambda 25.89\ \mu\text{m}$  emission line. Although the hard X-ray emission and  $[O\ IV]$  emission line are not directly related to the ionization state of the BLR clouds or dust temperature, their luminosities are expected to correlate with that of the accretion disk emission, and they would be far less obscured by the dust torus. Therefore, they could serve as luminosity indicators unbiased to dust obscuration (e.g., Meléndez et al. 2008; Diamond-Stanic et al. 2009; Rigby et al. 2009) and would be useful for estimating the radii of the BLR and innermost dust torus for type-2 AGNs and ultraluminous infrared galaxies. We enlarged the data for reverberation radii of the BLR by adding the results of the recent reverberation observations for  $H\beta$  emission lines (Bentz et al. 2006b, 2007, 2009a,b; Denney et al. 2010; Barth et al. 2011a,b; Grier et al. 2012b). The hard X-ray luminosity was obtained from the Swift BAT 58-Month Hard X-ray Survey (Baumgartner et al. submitted)<sup>11</sup>, and that of the  $[O\ IV]$  emission line was taken from previous research (Deo et al. 2007; Meléndez et al. 2008; Diamond-Stanic et al. 2009; Gallimore et al. 2010; Greene et al. 2010; Liu & Wang 2010; Tommasin et al. 2010).

As shown in Figures 13–15, the radii of the BLR ( $H\beta$ ) and innermost dust torus showed significant correlation with these luminosities, and the reverberation radius of the BLR was found to be systematically smaller than that of the innermost dust torus, as presented by Suganuma et al. (2006). In addition, we found that the reverberation radius of the innermost dust torus appeared to be systematically smaller than the interferometric radius of the innermost dust torus, as presented by Kishimoto et al. (2011). We then applied the regression analysis for the radius-luminosity relationship to quantitatively estimate their differences.

For the regression analysis, a linear equation,

$$\log r = \alpha + \beta \log L, \quad (5)$$

was adopted and fitted to the data, assuming  $\beta = 0.5$  in the same manner as that described in Section 4. We omitted the data for 3C 273, the most luminous target in Figures 13–15, from the fitting with the hard X-ray luminosities, because it is sometimes classified as a blazar, and its hard X-ray is apparently more luminous than the extension of the correlation of the interferometric radius of the innermost dust torus<sup>12</sup>. Rather than fitting

the data, the regression equation for the correlation of the dust reverberation radius and optical luminosity was converted from the result given in Section 4, and that for the correlation of the BLR reverberation radius and the optical luminosity was obtained from Bentz et al. (2009a). In addition, the regression line for the BLR radius and the  $[O\ IV]$  luminosity independently fitted by Greene et al. (2010) are presented for comparison.

The fitted parameters are presented in Table 9. We found that the BLR reverberation radius was smaller than the dust reverberation radius by 0.6–0.7 dex, or a factor of 4–5, and that the dust reverberation radius was smaller than the interferometric radius of the innermost dust torus by 0.2–0.4 dex, or about a factor of two.

The difference between the reverberation radius and interferometric radius of the dust torus observed in the same band can be understood by examining the difference between the response-weighted and flux-weighted radii (Kishimoto et al. 2011). Because the dust temperature in the torus is the highest at the inner boundary of the dust torus and becomes lower at larger radii, the flux-weighted radius would be larger than the inner boundary radius of the dust torus caused by the flux contribution from lower temperature dust at larger radii. In contrast, the reverberation radius analyzed by the CCF analysis would be more weighted on a larger amplitude of flux variation, which is expected to originate from a more compact emitting region or at smaller radii in the dust torus. Therefore, the reverberation radius is expected to be a better estimate for the inner boundary radius of the dust torus.

In addition to the factor of 4–5 difference for the mean reverberation radii of the innermost dust torus and BLR, a gap between their distributions is shown in Figure 13. However, on the basis of the following discussions, we suggest that these data do not necessarily indicate a gap of matter between the dust torus and the BLR.

The ionized gas clouds in the BLR are considered to be extended larger than the reverberation radius of Balmer emission lines. Clavel et al. (1991) conducted the reverberation mapping of various BELs in the UV spectrum for NGC 5548 and found that the lags tended to be shorter for higher ionization lines and longer for lower ionization lines. The lag times for the  $Si\ IV+O\ IV$ ,  $C\ III$ , and  $Mg\ II$  emission lines were larger by a factor of two or more for  $H\beta$  in similar epoch observations (Peterson et al. 2004). In addition, Hu et al. (2008) and Zhu et al. (2009) recently proposed a component of intermediate velocity width in conventional broad Balmer emission lines and suggested that the intermediate line region is located on the outer part of the BLR in the vicinity of the dust torus. Moreover, the ionized gas clouds of the BLR could be distributed at radii larger than the reverberation radius because the lag time corresponds to the centroid of the transfer function, which is considered to be the average radius of the distribution of the gas clouds (e.g., Horne 1999).

On the contrary, the dust with temperature higher than that of the black body radiation corresponding to the  $K$ -band wavelength is expected to be in a more inner location than that of the dust reverberation radius measured in the  $K$  band. Tomita et al. (2006) used the

calculating regressions of the radii with optical luminosity.

<sup>11</sup> <http://heasarc.gsfc.nasa.gov/docs/swift/results/bs58mon/>

<sup>12</sup> Because Kishimoto et al. (2011) noted that 3C 273 was in a quiescent state at the observing epoch of near-infrared interferometry and that the contribution of the synchrotron emission was expected to be small in the optical spectra, we included 3C 273 for

multicomponent fitting of the flux variation to find that the  $H$ -band flux variation for MCG +08–11–011 was followed by the  $K$ -band flux variation approximately 6 days later. Their results indicate that the reverberation radius in the  $H$  band was approximately 7% smaller than that in the  $K$  band obtained in this study. The same trend was reported by Tomita (2005) for additional AGNs. The  $I$ -band flux from the higher temperature of dust was detected by Sakata et al. (2010), who also used the multicomponent fitting of the flux variation. The dust temperature was estimated to be approximately 1700–2000 K for seven Seyfert galaxies, which is consistent with the sublimation temperature of graphite grains (Salpeter 1977).

Further, Koshida et al. (2009) discovered a rapid variation of dust lags obtained by the dust reverberation observation of NGC 4151. Because this variation was found to be significantly faster than the dynamical timescale at the radii of the BLR and inner dust torus, they concluded that the formation and destruction of dust grains in the gas clouds changed the radius of the innermost dust torus. These results suggest that the gas clouds are distributed continuously and that the inner boundary of the dust torus is determined by the sublimation of the hottest grains in the clouds (Netzer & Laor 1993), which were located between the reverberation radii of the  $K$ -band dust emission region and the  $H\beta$  BLR.

Mor et al. (2009) reported near-infrared excess emission in the infrared SEDs of AGNs that could not be explained by the components of emission from a clumpy dust torus model (Nenkova et al. 2002, 2008) or by the dusty narrow emission-line region (NLR). Mor & Netzer (2012) introduced a gas cloud with hot pure-graphite grains to account for such excess emission and constructed an SED model consisting of a hot-dust cloud, a clumpy dust torus, and a dusty NLR to fit the infrared SED of type-1 AGNs. Figure 13 shows the location of the hot-dust clouds obtained from such fittings reported by Mor & Netzer (2012). Indeed, the hot dust clouds were located between the two reverberation radii, which also suggests that the inner radius of the dust torus is smaller than the  $K$ -band dust reverberation radius but larger than the Balmer-line reverberation radius.

The inner radius of the dust torus was expected to be smaller than that of Equation (1), assuming  $T_{\text{sub}} = 1500$  K and  $a = 0.05 \mu\text{m}$ , by a factor of more than  $\sim 3$ . However, a higher sublimation temperature is probable as described. In addition, a larger grain size of  $a \approx 0.1 \mu\text{m}$  could be adopted on the basis of the analysis of reddening curves for quasars (Gaskell et al. 2004). By assuming  $T_{\text{dust}} = 1700$  K for the dust temperature that was evaluated from the NIR colors of the variable flux component for Seyfert 1 galaxies (Tomita 2005; Tomita et al. 2006), and  $a = 0.1 \mu\text{m}$  for the grain size, the sublimation radius predicted by Equation (1) can be written as  $\log R_{\text{sub}}/\text{pc} = -0.80 + 0.5 \log (L_V/10^{44} \text{ erg s}^{-1})$ , where  $L_{\text{UV}} = 6L_V$  (Kishimoto et al. 2007), which was found to be close to the  $K$ -band dust reverberation radius. It should be noted that  $L_{\text{UV}}$  in Equation (1) is an effective luminosity of the UV-optical continuum emission multiplied by the wavelength-dependent absorption efficiency of dust grains. Therefore, a detailed calculation of radiation equilibrium in dusty clouds is necessary and will

appear in a forthcoming paper.

## 6. SUMMARY

We presented the results of a dust reverberation survey for 17 nearby Seyfert 1 galaxies, which provides the largest homogeneous data collection for the radius of the innermost dust torus. For all targets, long-term monitoring observations in optical and near-infrared wavelengths showed a delayed response of the  $K$ -band light curve after that of the  $V$  band. The minor contribution of the accretion disk in the  $K$ -band flux was subtracted to derive the variation of the dust torus emission, and the CCF analysis was applied to obtain 49 measurements of reverberation lags for the innermost dust torus. The optical luminosity of the continuum emission from the accretion disk was estimated by subtracting the host-galaxy and narrow-line flux contributions in the  $V$ -band fluxes. We found that the reverberation lags for the innermost dust torus strongly correlated with the optical luminosity in the range of  $M_V = -16$  to  $-22$  mag. We applied the regression analysis to our new data to obtain the correlation of  $\log \Delta t$  (days)  $= -2.11 - 0.2M_V$  or  $\log c\Delta t$  (pc)  $= -0.88 + 0.5(L_V/10^{44} \text{ ergs s}^{-1})$ , assuming the slope of  $\Delta t \propto L^{0.5}$  to be same as that reported in previous studies. The intrinsic scatter of the correlation was estimated to be approximately 0.13 dex, and its possible origins were discussed. The difference in internal extinction and the delayed response of changes in lag times to the flux variations could have partly contributed to the intrinsic scatter; however, we could not detect systematic changes in the lag-luminosity correlation with the subclass of the Seyfert type and the Eddington ratio.

Furthermore, we compared our results with the radius-luminosity correlations for the near-infrared interferometry and BLR reverberation. In addition to that with the optical luminosity, we examined such correlations with the hard X-ray (14–195 keV) and  $[\text{O IV}]\lambda 25.89 \mu\text{m}$  emission-line luminosities, which are known as isotropic luminosity indicators and are applicable to obscured AGNs. We found that the interferometric radius in the  $K$  band was systematically larger than the reverberation radius in the same band by approximately 0.3 dex, which could be interpreted as the difference between the flux-weighted radius and the response-weighted radius, as suggested by Kishimoto et al. (2011). We suggest that the reverberation radius provides a better estimate for the inner boundary radius of the dust torus.

As expected from the unified scheme of the Seyfert type of AGNs, the BLR reverberation radius was found to be systematically smaller than the dust reverberation radius, as reported by Suganuma et al. (2006), with a difference of approximately 0.6–0.7 dex. However, we suggest that gas clouds with the hottest dust, and those emitting BELs of lower ionization species or intermediate lines, are located between them, wherein the inner radius of the dust torus is determined by the sublimation of dust grains. The higher dust temperature of  $T_{\text{dust}} \approx 1700$  K and the larger grain size of  $a \approx 0.1 \mu\text{m}$  are preferred for the parameters of the dust sublimation radius expressed in Equation (1); however, detailed calculation of radiation equilibrium in dusty clouds is desired.

We thank the staff at the Haleakala Observatories for

their help with facility maintenance. This research has been partly supported by the Grant-in-Aids of Scientific Research (10041110, 10304014, 11740120, 12640233, 14047206, 14253001, 14540223, 16740106, 22540247, 25287062, and the COE Research (07CE2002) of the Ministry of Education, Science, Culture and Sports of Japan.

## REFERENCES

- Abramowicz, M. A., Czerny, B., Lasota, J. P., & Szuszkiewicz, E. 1988, *ApJ*, 332, 646
- Antonucci, R. R. J., & Miller, J. S. 1985, *ApJ*, 297, 621
- Antonucci, R. 1993, *ARA&A*, 31, 473
- Baribaud, T., Alloin, D., Glass, I., & Pelat, D. 1992, *A&A*, 256, 375
- Barth, A. J., Nguyen, M. L., Malkan, M. A. et al. 2011, *ApJ*, 732, 121
- Barth, A. J., Pancoast, A., Thorman, S. J. et al. 2011, *ApJ*, 743, L4
- Barvainis, R. 1987, *ApJ*, 320, 537
- Barvainis, R. 1992, *ApJ*, 400, 502
- Bentz, M. C., Denney, K. D., Cackett, E. M. et al. 2006, *ApJ*, 651, 775
- Bentz, M. C., Peterson, B. M., Pogge, R. W., Vestergaard, M., & Onken, C. A. 2006, *ApJ*, 644, 133
- Bentz, M. C., Denney, K. D., Cackett, E. M. et al. 2007, *ApJ*, 662, 205
- Bentz, M. C., Peterson, B. M., Netzer, H., Pogge, R. W., & Vestergaard, M. 2009, *ApJ*, 697, 160
- Bentz, M. C., Walsh, J. L., Barth, A. J., et al. 2009, *ApJ*, 705, 199
- Boroson, T. A., & Meyers, K. A. 1992, *ApJ*, 397, 442
- Cackett, E. M., Horne, K., & Winkler, H. 2007, *MNRAS*, 380, 669
- Clavel, J., Wamsteker, W., & Glass, I. S. 1989, *ApJ*, 337, 236
- Clavel, J., Reichert, G. A., Alloin, D., et al. 1991, *ApJ*, 366, 64
- Collier, S., & Peterson, B. M. 2001, *ApJ*, 555, 775
- Denney, K. D., Bentz, M. C., Peterson, B. M., et al. 2006, *ApJ*, 653, 152
- Denney, K. D., Peterson, B. M., Pogge, R. W., et al. 2010, *ApJ*, 721, 715
- Deo, R. P., Crenshaw, D. M., Kraemer, S. B., Dietrich, M., Elitzur, M., Teplitz, H., Turner, T. J. 2007, *ApJ*, 671, 124
- Deo, R. P., Richards, G. T., Nikutta, R., et al. 2011, *ApJ*, 729, 108
- Diamond-Stanic, A. M., Rieke, G. H., & Rigby, J. R. 2009, *ApJ*, 698, 623
- Dietrich, M., Peterson, B. M., Grier, C. J., et al. 2012, *ApJ*, 757, 53
- Doroshenko, V. T., Sergeev, S. G., Klimanov, S. A., Pronik, V. I., & Efimov, Yu. S. 2012, *MNRAS*, 426, 416
- Du, P., Hu, C., Lu, K.-X., et al. 2014, *ApJ*, 782, 45
- Dullemond, C. P. & van Bemmelen, I. M. 2005, *A&A*, 436, 47
- Edri, H., Rafter, S. E., Chelouche, D., Kaspi, S., & Behar, E. 2012, *ApJ*, 756, 73
- Elitzur, M. 2012, *ApJ*, 747, L33
- Enya, K., Yoshii, Y., Kobayashi, Y., et al. 2002, *ApJS*, 141, 31
- Gallimore, J. F., Yzaguirre, A., Jakoboski, J., Stevenosky, M. J., Axon, D. J., Baum, S. A., Buchanan, C. L., Elitzur, M., Elvis, M., O'Dea, C. P., & Robinson, A. 2010, *ApJS*, 187, 172
- Gaskell, C. M., Goosmann, R. W., Antonucci, R. R. J., & Whysong, D. H. 2004, *ApJ*, 616, 147
- Gibbons, R. A., Fruchter, A. S., & Bothun, G. D. 2001, *AJ*, 121, 649
- Glass, I. S. 1992, *MNRAS*, 256, 23P
- Glass, I. S. 2004, *MNRAS*, 350, 1049
- Greene, J. E., Hood, C. E., Barth, A. J., Bennert, V. N., Bentz, M. C., Filippenko, A. V., Gates, E., Malkan, M. A., Treu, T., Walsh, J. L., & Woo, J.-H. 2010, *ApJ*, 723, 409
- Grier, C. J., Peterson, B. M., Horne, K., et al. 2013, *ApJ*, 764, 47
- Grier, C. J., Peterson, B. M., Pogge, R. W., et al. 2012, *ApJ*, 744, 4
- Grier, C. J., Peterson, B. M., Pogge, R. W., et al. 2012, *ApJ*, 755, 60
- Hönig, S. F., Beckert, T., Ohnaka, K., Weigelt, G. 2006, *A&A*, 452, 459
- Horne, K. 1999, in *ASP Conf. Ser. 162, Quasars and Cosmology*, ed. G. Ferland & J. Baldwin (San Francisco, CA: ASP), 189
- Hu, C., Wang, J.-M., Ho, L. C., Chen, Y.-M., Bian, W.-H., & Xue, S.-J. 2008, *ApJ*, 683, L115
- Hunt, L. K., Mannucci, F., Testi, L., et al. 1998, *AJ*, 115, 2594
- Jefferys, W. H. 1980, *AJ*, 85, 177
- Kaspi, S., Maoz, D., Netzer, H., et al. 1996, *ApJ*, 470, 336
- Kaspi, S., Smith, P. S., Netzer, H., Maoz, D., Jannuzi, B. T., & Givon, U. 2000, *ApJ*, 533, 631
- Kaspi, S., Maoz, D., Netzer, H., et al. 2005, *ApJ*, 629, 61
- Kawaguchi, T., & Mori, M. 2010, *ApJ*, 724, L183
- Kawaguchi, T., & Mori, M. 2011, *ApJ*, 737, 105
- Kawakatu, N., & Ohsuga, K. 2012, *MNRAS*, 417, 2562
- Kelly, B. C., Bechtold, J., & Siemiginowska, A. 2009, *ApJ*, 698, 895
- Kishimoto, M., Hönig, S. F., Beckert, T., & Weigelt, G. 2007, *A&A*, 476, 713
- Kishimoto, M., Antonucci, R., Blaes, O., Lawrence, A., Boisson, C., Albrecht, M., Leipski, C. 2008, *Nature*, 454, 492
- Kishimoto, M., Hönig, S. F., Antonucci, R., et al. 2009, *A&A*, 507, L57
- Kishimoto, M., Hönig, S. F., Antonucci, R., et al. 2011, *A&A*, 536, A78
- Kishimoto, M., Hönig, S. F., Antonucci, R., et al. 2013, *ApJ*, 775, L36
- Kobayashi, Y., Sato, S., Yamashita, T., Shiba, H., & Takami, H., 1993, *ApJ*, 404, 94
- Kobayashi, Y., et al., 1998, *Proc. SPIE*, 3352, 120
- Kobayashi, Y., Yoshii, Y., Peterson, B. A., Minezaki, T., Enya, K., Suganuma, M., & Yamamuro, T., 1998, *Proc. SPIE*, 3354, 769
- Koshida, S., Yoshii, Y., Kobayashi, Y., et al. 2009, *ApJ*, 700, L109
- Kozłowski, S., Kochanek, C. S., Udalski, A., et al. 2010, *ApJ*, 708, 927
- Krolik, J. H., & Begelman, M. C. 1988, *ApJ*, 329, 702
- Landolt, A. U. 1992, *AJ*, 104, 372
- Landt, H., Bentz, M. C., Peterson, B. M., et al. 2011, *MNRAS*, 413, L106
- Lira, P., Arévalo, P., Uttley, P., McHardy, I., Breedt, E. 2011, *MNRAS*, 415, 1290
- Liu, T., & Wang, J.-X. 2010, *ApJ*, 725, 2381
- MacLeod, C. L., Ivezić, Ž., Sesar, B., et al. 2012, *ApJ*, 753, 106
- MacLeod, C. L., Ivezić, Ž., Kochanek, C. S., et al. 2010, *ApJ*, 721, 1014
- Maoz, D., & Netzer, H. 1989, *MNRAS*, 236, 21
- Marziani, P., Sulentic, J. W., Zamanov, R., et al. 2003, *ApJS*, 145, 199
- Masters, K. L., Springob, C. M., Haynes, M. P., & Giovanelli, R. 2006, *ApJ*, 653, 861
- Meléndez, M., Kraemer, S. B., Armentrout, B. K., Deo, R. P., Crenshaw, D. M., Schmitt, H. R., Mushotzky, R. F., Tueller, J., Markwardt, C. B., & Winter, L. 2008, *ApJ*, 682, 94
- Miller, J. S., & Goodrich, R. W. 1990, *ApJ*, 355, 456
- Minezaki, T., Yoshii, Y., Kobayashi, Y., et al. 2004, *ApJ*, 600, L35
- Minezaki, T., Yoshii, Y., Kobayashi, Y., et al. 2006, *ApJ*, 643, L5
- Mor, R., Netzer, H., & Elitzur, M. 2009, *ApJ*, 705, 298
- Mor, R., & Netzer, H. 2012, *MNRAS*, 420, 526
- Mould, J. R., Huchra, J. P., Freedman, W. L., et al. 2000, *ApJ*, 529, 786, with an erratum
- Nelson, B. O. 1996, *ApJ*, 465, L87
- Nelson, B. O. 1996, Ph.D. dissertation, University of California, Los Angeles
- Nelson, B. O., & Malkan, M. A. 2001, in *ASP Conf. Ser. 224, Probing the Physics of Active Galactic Nuclei*, ed. B. M. Peterson, R. W. Pogge, & R. S. Polidan (San Francisco, CA: ASP), 141
- Neškova, M., Ivezić, Ž., & Elitzur, M. 2002, *ApJ*, 570, L9
- Neškova, M., Sirocky, M. M., Nikutta, R., Ivezić, Ž., & Elitzur, M. 2008, *ApJ*, 685, 160
- Netzer, H., & Laor, A. 1993, *ApJ*, 404, L51
- Oknyanskij, V. L. 1993, *Astronomy Letters*, 19, 416
- Oknyanskij, V. L., Lyuty, V. M., Taranova, O. G., & Shenavrin, V. I. 1999, *Astronomy Letters*, 25, 483
- Oknyanskij, V. L., & Horne, K. 2001, in *ASP Conf. Ser. 224, Probing the Physics of Active Galactic Nuclei*, ed. B. M. Peterson, R. W. Pogge, & R. S. Polidan (San Francisco, CA: ASP), 149
- Onken, C. A., Peterson, B. M., Dietrich, M., Robinson, A., & Salamanca, I. M. 2003, *ApJ*, 585, 121
- Osterbrock, D. E., & Martel, A. 1993, *ApJ*, 414, 552
- Peng, C. Y., Ho, L. C., Impey, C. D., & Rix, H.-W. 2002, *AJ*, 124, 266
- Peterson, B. M., Wanders, I., Horne, K., Collier, S., Alexander, T., Kaspi, S., & Maoz, D. 1998, *PASP*, 110, 660
- Peterson, B. M., 2001, in *Advanced Lectures on the Starburst-AGN Connection*, ed. I. Aretxaga, D. Kunth, & Mújica (Singapore: World Scientific), 3
- Peterson, B. M., Ferrarese, L., Gilbert, K. M., et al. 2004, *ApJ*, 613, 682
- Pier, E. A. & Krolik, J. H. 1992, *ApJ*, 401, 99
- Pott, J.-U., Malkan, M. A., Elitzur, M., Ghez, A. M., Herbst, T. M., Schödel, R., & Woillez, J. 2010, *ApJ*, 715, 736
- Pozo Nuñez, F., Haas, M., Chini, R., Ramolla, M., Westhues, C., Steenbrugge, K., Kaderhandt, L., Drass, H., Lemke, R., & Murphy, M. 2014, *A&A*, 561, L8
- Press, W. H., Rybicki, G. B., & Hewitt, J. N. 1992, *ApJ*, 385, 404
- Radburn-Smith, D. J., Lucey, J. R., & Hudson, M. J. 2004, *MNRAS*, 355, 1378
- Rafter, S. E., Kaspi, S., Behar, E., Kollatschny, W., & Zetzl, M. 2011, *ApJ*, 741, 66
- Rees, M. J., Silk, J. I., Werner, M. W., Wickramasinghe, N. C. 1969, *Nature*, 223, 788

- Rigby, J. R., Diamond-Stanic, A. M., & Aniano, G. 2009, *ApJ*, 700, 1878
- Rybicki, G. B., & Kleyana, J. T. 1994, in *ASP Conf. Ser.* 69, Reverberation mapping of the broad-line region in active galactic nuclei, ed. P. M. Gondhalekar, K. Horne, & B. M. Peterson (San Francisco, CA: ASP), 85
- Rybicki, G. B., & Press, W. H. 1992, *ApJ*, 398, 169
- Sakata, Y., Minezaki, T., Yoshii, Y., Kobayashi, Y., Koshida, S., Aoki, T., Enya, K., Tomita, H., Suganuma, M., Katsuno Uchimoto, Y., & Sugawara, S. 2010, *ApJ*, 711, 461
- Salpeter, E. E. 1977, *ARA&A*, 15, 267
- Schartmann, M., Meisenheimer, K., Camenzind, M., Wolf, S., Henning, T. 2005, *A&A*, 437, 861
- Schartmann, M., Meisenheimer, K., Camenzind, M., Wolf, S., Tristram, K. R. W., Henning, T. 2008, *A&A*, 482, 67
- Schlegel, D. J., Finkbeiner, D. P., & Davis, M. 1998, *ApJ*, 500, 525
- Schmitt, H. R., Donley, J. L., Antonucci, R. R. J., et al. 2003, *ApJ*, 597, 768
- Shakura, N. I., & Sunyaev, R. A. 1973, *A&A*, 24, 337
- Shapovalova, A. I., Popović, L. Č., Burenkov, A. N., et al. 2013, *A&A*, 559, A10
- Sitko, M. L., Sitko, A. K., Siemiginowska, A., & Szczerba, R. 1993, *ApJ*, 409, 139
- Spergel, D. N., Bean, R., Doré, O., et al. 2007, *ApJS*, 170, 377
- Suganuma, M., Yoshii, Y., Kobayashi, Y., et al. 2004, *ApJ*, 612, L113
- Suganuma, M., Yoshii, Y., Kobayashi, Y., et al. 2006, *ApJ*, 639, 46
- Storey, P. J., & Zeppen, C. J. 2000, *MNRAS*, 312, 813
- Swain, M., Vasisht, G., Akeson, R., et al. 2003, *ApJ*, 596, L163
- Telesco, C. M., Becklin, E. E., Wynn-Williams, C. G., & Harper, D. A. 1984, *ApJ*, 282, 427
- Tomita, H. 2005, Doctoral Dissertation, The University of Tokyo
- Tomita, H., Yoshii, Y., Kobayashi, Y., Minezaki, T., Enya, K., Suganuma, M., Aoki, T., Koshida, S., & Yamauchi, M. 2006, *ApJ*, 652, L13
- Tommasin, S., Spinoglio, L., Malkan, M. A., & Fazio, G. 2010, *ApJ*, 709, 1257
- Véron-Cetty, M.-P., & Véron, P. 2001, *A&A*, 374, 92
- Véron-Cetty, M.-P., & Véron, P. 2010, *A&A*, 518, A10
- Wandel, A., Peterson, B. M., & Malkan, M. A. 1999, *ApJ*, 526, 579
- Watkins, R. 1997, *MNRAS*, 292, L59
- Weigelt, G., Hofmann, K.-H., Kishimoto, M., Hönig, S., Schertl, D., Marconi, A., Millour, F., Petrov, R., Fraix-Burnet, D., Malbet, F., Tristram, K., Vannier, M. 2012, *A&A*, 541, L9
- White, R. J., & Peterson, B. M. 1994, *PASP*, 106, 879
- Whittle, M. 1992, *ApJS*, 79, 49
- Wilhite, B. C., Vanden Berk, D. E., Kron, R. G., Schneider, D. P., Pereyra, N., Brunner, R. J., Richards, G. T., & Brinkmann, J. V. 2005, *ApJ*, 633, 638
- Winkler, H., Glass, I. S., van Wyk, F., et al. 1992, *MNRAS*, 257, 659
- Yoshii, Y. 2002, in *Proceedings of the 5th RESCEU International Symposium on New Trends in Theoretical and Observational Cosmology*, ed. K. Sato & T. Shiromizu (Tokyo: Universal Academy Press), 235
- Yoshii, Y., Kobayashi, Y., & Minezaki, T. 2003, *Bulletin of the American Astronomical Society*, 35, 752
- Zhang, X.-G. 2013, *MNRAS*, 431, L112
- Zhang, X.-G. 2013, *MNRAS*, 434, 2664
- Zhu, L., Zhang, S. N., & Tang, S. 2009, *ApJ*, 700, 1173
- Zu, Y., Kochanek, C. S., & Peterson, B. M. 2011, *ApJ*, 735, 80
- Zu, Y., Kochanek, C. S., Kozłowski, S., & Udalski, A. 2013, *ApJ*, 765, 106

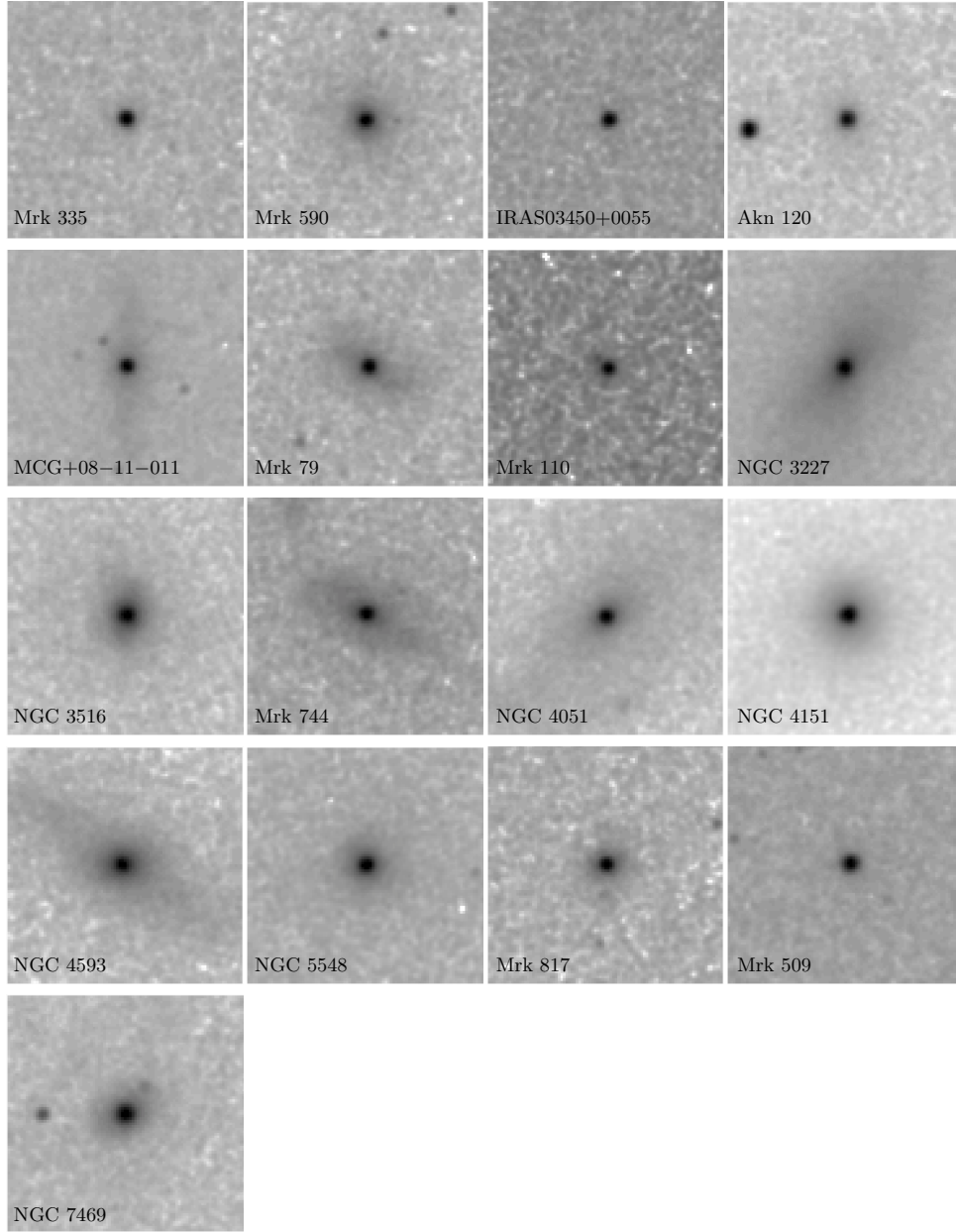


FIG. 1.— Portrait images of the target Seyfert galaxies in the  $K$  band (taken from the Two Micron All Sky Survey). The field of view of the image is  $1.5 \times 1.5$  arcmin<sup>2</sup>, which represents that of the MAGNUM MIP camera for this study. The image intensity levels are displayed in logarithmic scale.

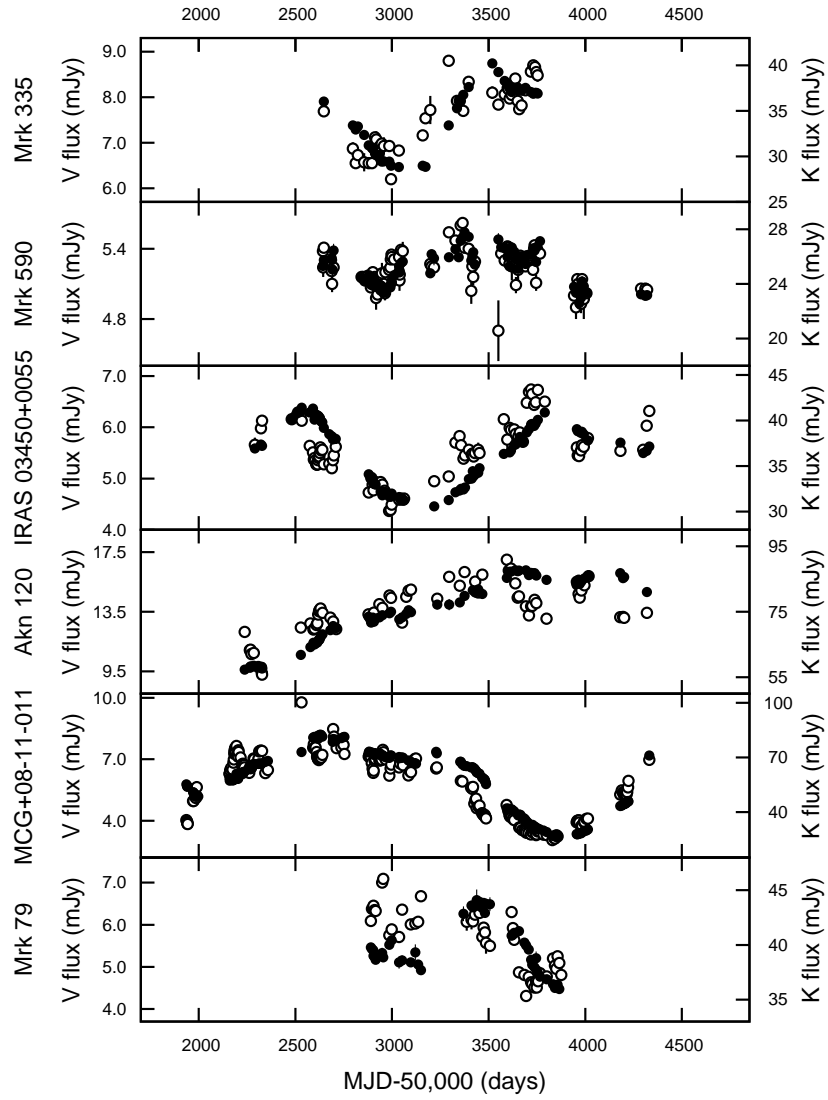


FIG. 2.— V-band (open circles) and K-band (filled circles) light curves of Mrk 335, Mrk 590, IRAS 03450+0055, Akn 120, MCG +08-11-011, and Mrk 79. Correction for the Galactic extinction has not been applied to the light curves, and the fluxes from the host galaxy and narrow emission lines have not been subtracted.

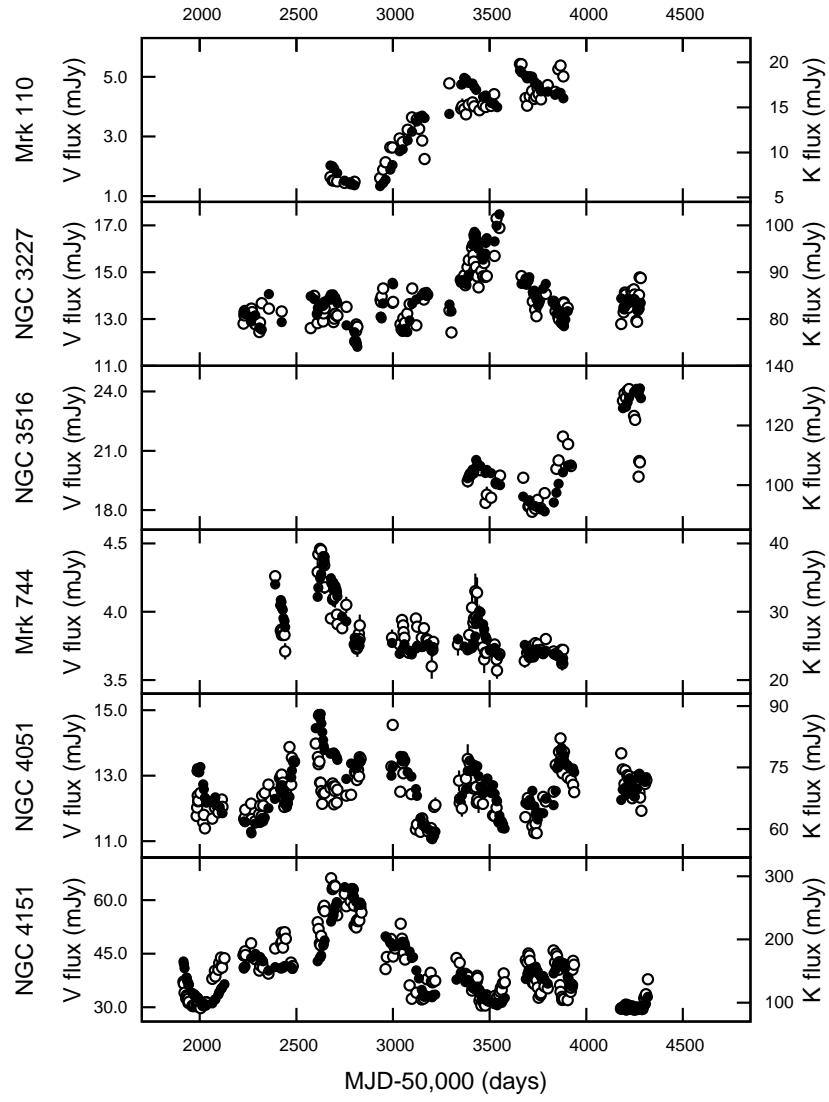


FIG. 3.— V-band and K-band light curves of Mrk 110, NGC 3227, NGC 3516, Mrk 744, NGC 4051, and NGC 4151. Symbols and others are the same as Figure 2.



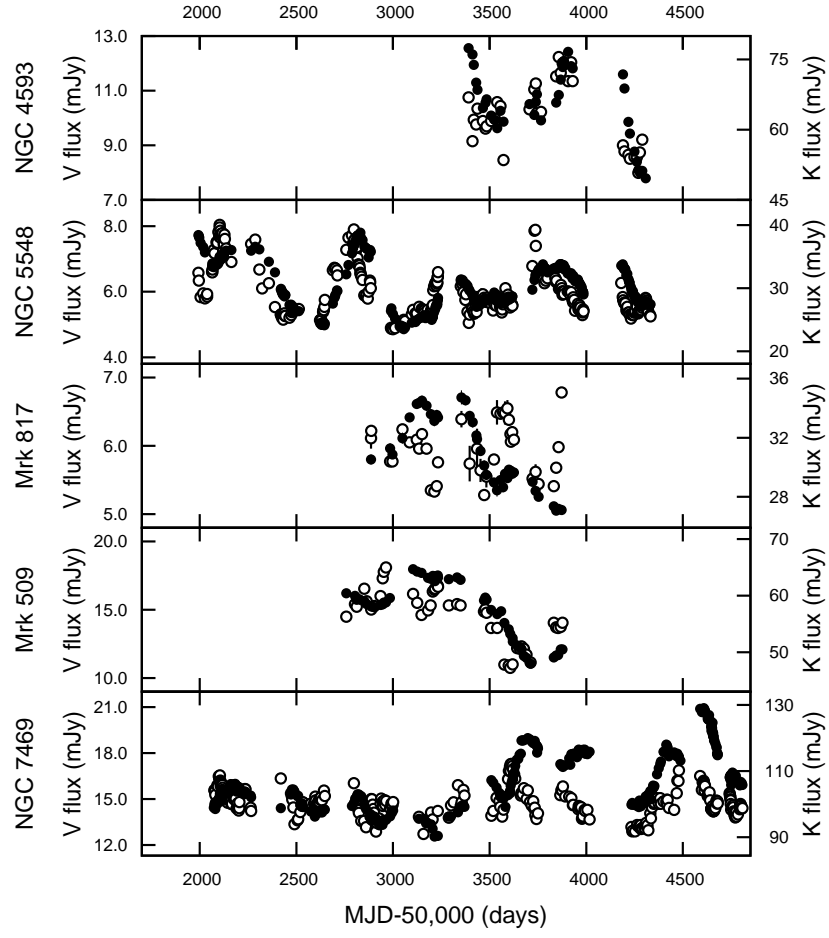


FIG. 4.— V-band and K-band light curves of NGC 4593, NGC 5548, Mrk 817, Mrk 509, and NGC 7469. Symbols and others are the same as Figure 2.

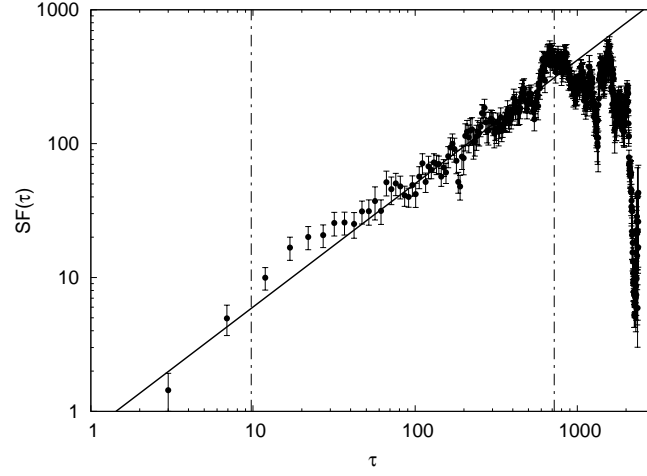


FIG. 5.— Structure function of the V-band flux variation of NGC 4151. The filled circle shows the data point for each bin of the time interval  $\tau$  calculated from the observed light curve; the solid line shows the regression line in a power-law form in the range of the time interval in which the structure function is considered to be significant (between the two dot-dashed lines).

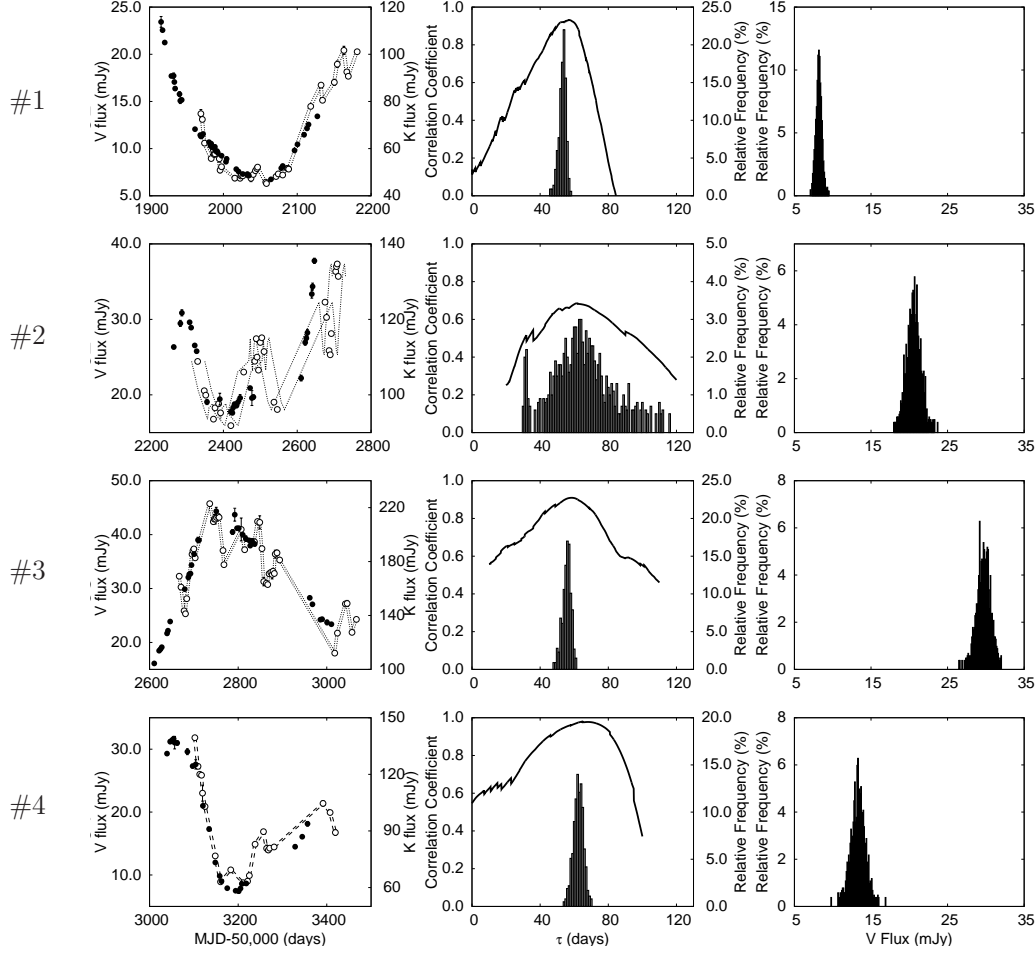


FIG. 6.— Results of the cross-correlation function (CCF) analysis of NGC 4151 at different epochs (#1-#4). Left panels show the  $K$ -band (filled circles) and  $V$ -band (open circles) light curves. The latter have shifted according to the lag time between them,  $\Delta t_K$ , as derived from the CCF analysis. Dotted lines show the  $V$ -band light curves shifted by  $\Delta t_K$  plus and minus its error. Middle panels show the CCF of the observed light curves (solid line) and the cross-correlation centroid distribution (CCCD) derived from Monte Carlo simulation (histogram) for respective epochs. Right panels show the distribution of the average  $V$ -band flux  $\bar{f}_V$  derived from the Monte Carlo simulation.

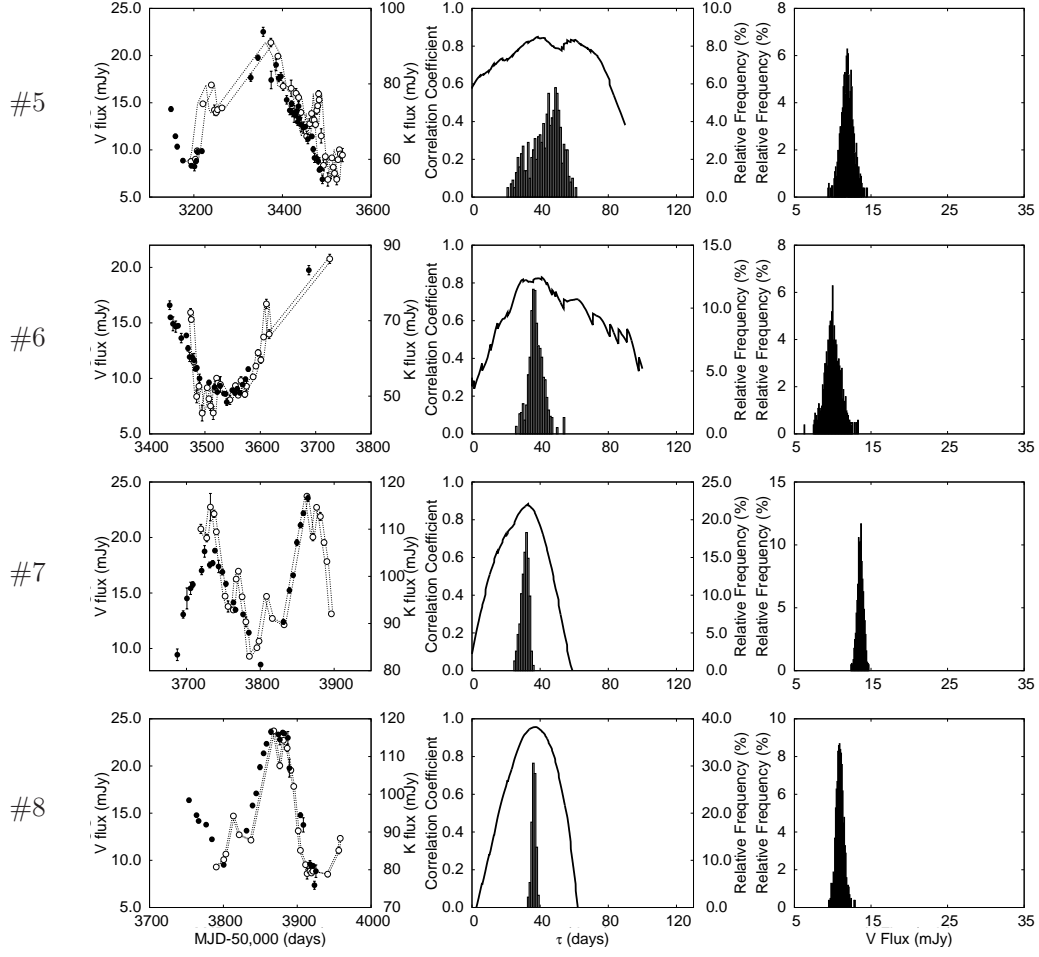


FIG. 7.— Results of the CCF analysis of NGC 4151 at different epochs (#5–#8). Symbols and others are the same as Figure 6.

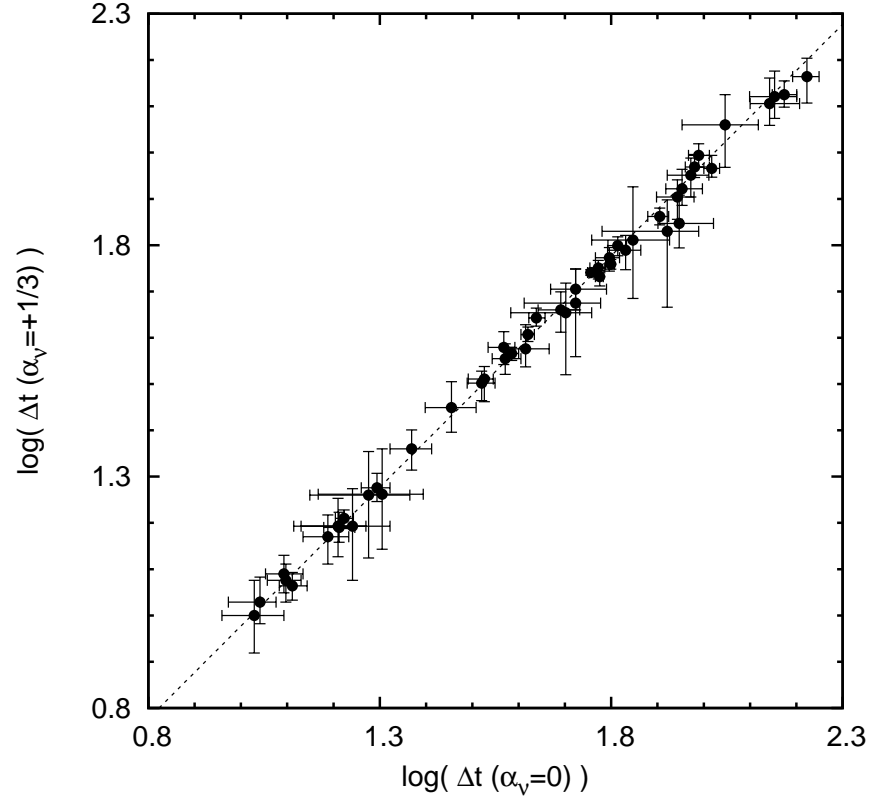


FIG. 8.— Comparison of the dust lags  $\Delta t_K$  obtained by the CCF analysis assuming  $\alpha_{\nu} = 0$  and  $+1/3$  for subtraction of the accretion-disk component in the  $K$ -band flux. The dashed line represents the best-fit regression line.

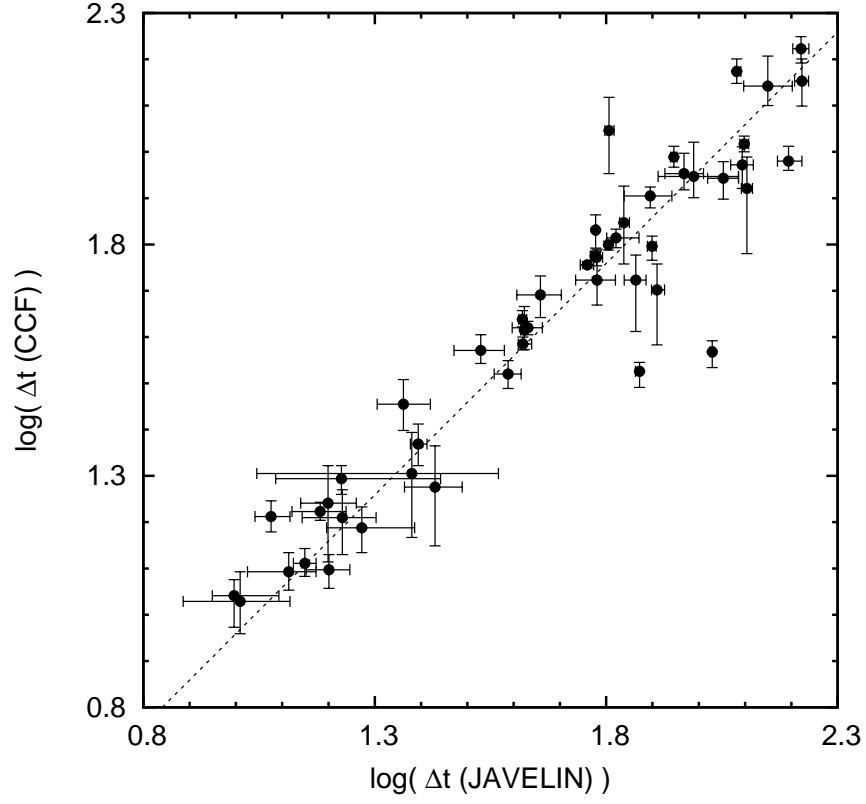


FIG. 9.— Comparison of the dust lags  $\Delta t_K$  obtained by using the CCF analysis and JAVELIN (assuming  $\alpha_\nu = 0$  for the subtraction of the accretion-disk component in the  $K$ -band flux). The dashed line represents the best-fit regression line.

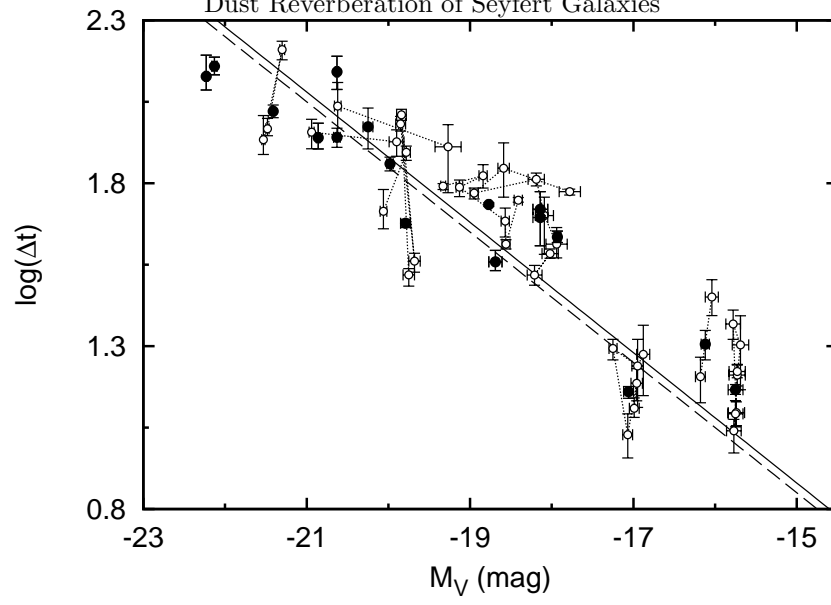


FIG. 10.— Lag times between the  $V$ -band and  $K$ -band light curves plotted against the  $V$ -band absolute magnitude. Open circles represent 49 measurements of the lag times (obtained by the CCF analysis assuming  $\alpha_\nu = 0$  for the subtraction of the accretion-disk component in the  $K$ -band flux) and  $V$ -band absolute magnitude, and the data points are connected with dotted lines for the same target. Filled circles represent the weighted averaged data for 17 individual target active galactic nuclei (AGNs). Solid and dashed lines represent the best-fit regression lines for the data obtained by the CCF analysis assuming  $\alpha_\nu = 0$  and  $\alpha_\nu = 1/3$  respectively. The lag times were corrected for the time dilation according to the object redshift.

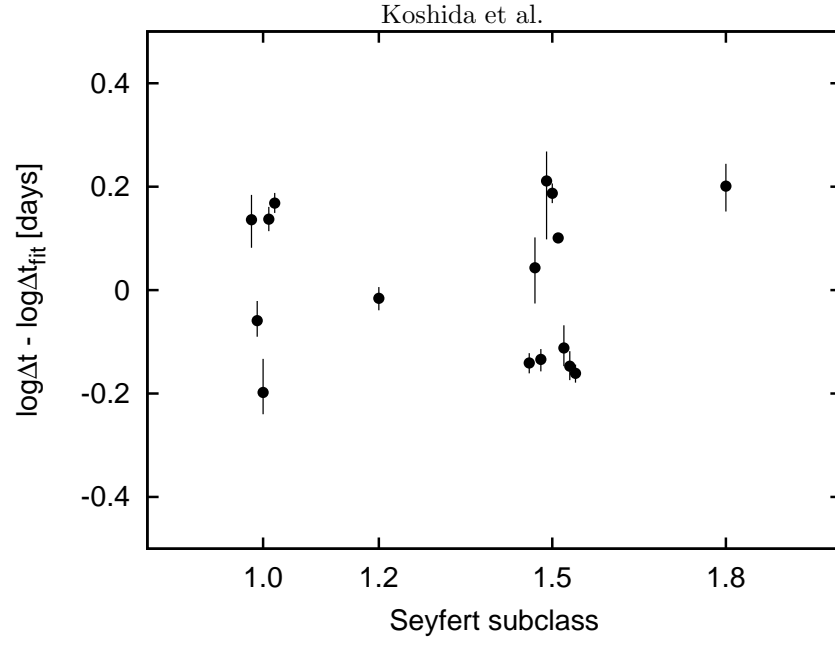


FIG. 11.— Residual of the dust lag from the best-fit regression line plotted against the subclass of the Seyfert type (obtained by the CCF analysis assuming  $\alpha_\nu = 0$  for the subtraction of the accretion-disk component in the  $K$ -band flux).



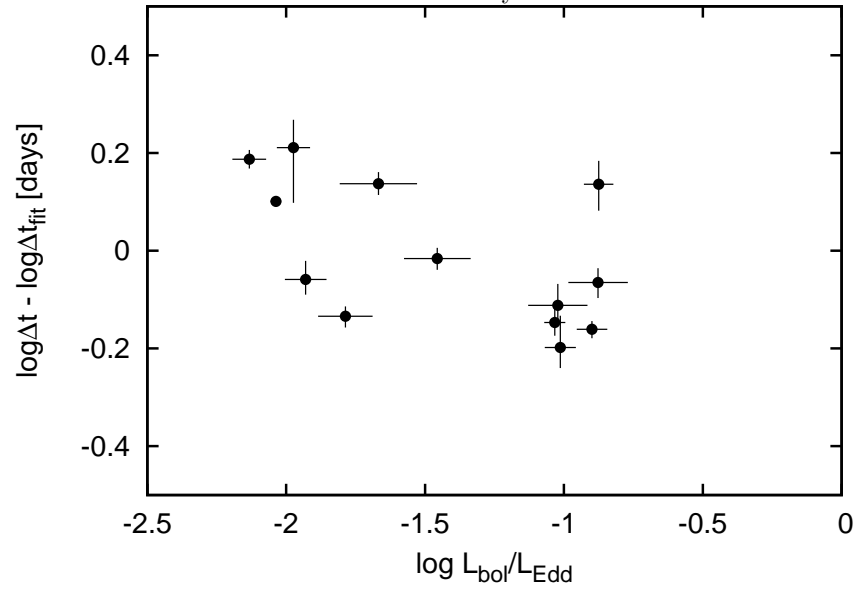


FIG. 12.— Residual of the dust lag from the best-fit regression line plotted against the Eddington ratio (obtained by the CCF analysis assuming  $\alpha_{\nu} = 0$  for the subtraction of the accretion-disk component in the  $K$ -band flux).

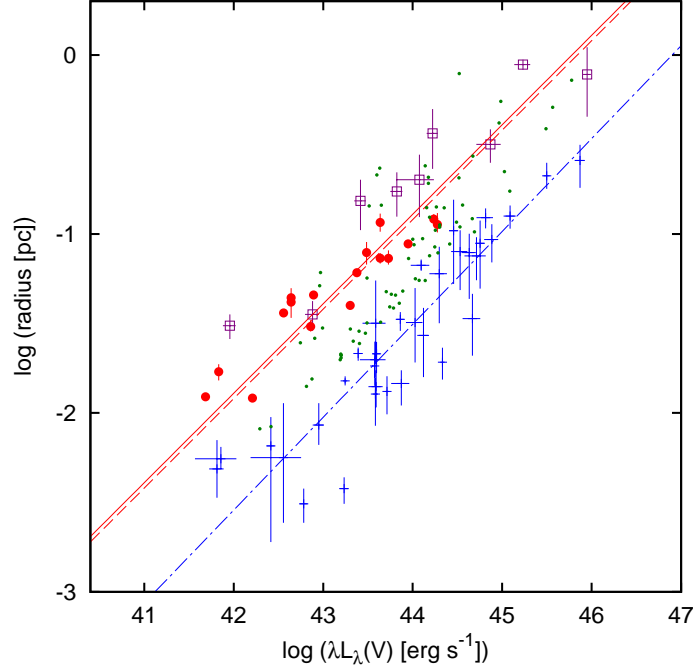


FIG. 13.— Radii of the innermost dust torus and the broad emission-line region (BLR) plotted against the  $V$ -band luminosity. Filled circles (colored red in the online version) represent the  $K$ -band reverberation radii of our results (obtained by the CCF analysis assuming  $\alpha_\nu = 0$  for the subtraction of the accretion-disk component in the  $K$ -band flux); open squares (colored purple in the online version) represent the  $K$ -band interferometric radii obtained from Kishimoto et al. (2011) and Weigelt et al. (2012), and crosses (colored blue in the online version) represent the reverberation radii of broad Balmer emission lines obtained from Bentz et al. (2009a). Solid and dashed lines (colored red in the online version) represent the best-fit regression lines for the  $K$ -band reverberation radii for the data obtained by the CCF analysis assuming  $\alpha_\nu = 0$  and  $\alpha_\nu = 1/3$ , respectively, and the dot-dashed line (colored blue in the online version) represents the best-fit regression line for the Balmer-line reverberation radii reported by Bentz et al. (2009a). Dots (colored green in the online version) represent the radii of the location of the hot-dust clouds obtained from the spectral energy distribution (SED) fitting of type-1 active galactic nuclei (AGNs) reported by Mor & Netzer (2012).

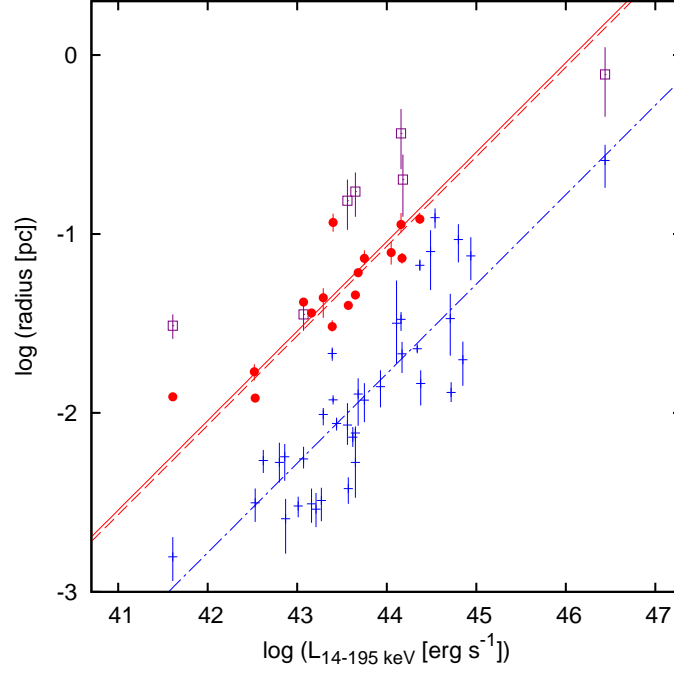


FIG. 14.— Radii of the innermost dust torus and the broad emission-line region (BLR) plotted against the hard X-ray (14–195 keV) luminosity. Symbols are the same as Figure 13 but for the data of the reverberation radii of broad Balmer emission lines taken from more literature (Bentz et al. 2006b, 2007, 2009a,b; Denney et al. 2010; Barth et al. 2011a,b; Grier et al. 2012b).

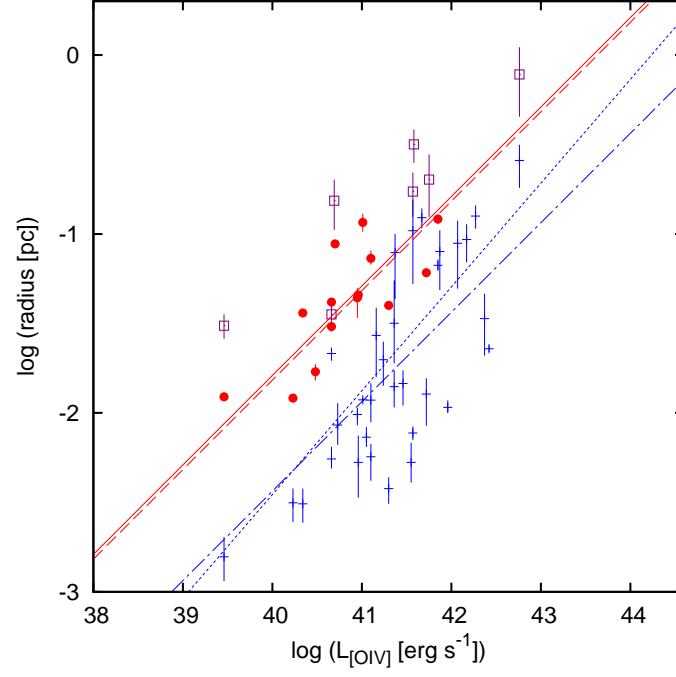


FIG. 15.— Radii of the innermost dust torus and the broad emission-line region (BLR) plotted against the [O IV] emission-line luminosity. Symbols are the same as Figure 14 but the dotted line (colored blue in the online version) represents the best-fit regression line for the Balmer-line reverberation radii presented by Greene et al. (2010).

TABLE 1  
LIST OF TARGET ACTIVE GALACTIC NUCLEI

Name	R.A. (J2000)	Decl. (J2000)	Diameter <sup>a</sup> (arcmin)	$z$	$M_V$ <sup>b</sup> (mag)	Seyfert type	Ref.	$\log(M_{\text{BH}}/M_{\odot})$	Ref.
Mrk 335	00 06 19.5	+20 12 10.5	$0.3 \times 0.3$	0.0258	-22.10	1.2	1	$7.40 \pm 0.05$	3
Mrk 590	02 14 33.6	-00 46 00.1	$1.1 \times 1.0$	0.0264	-22.19	1.2	2	$7.68 \pm 0.07$	4
IRAS 03450+0055	03 47 40.2	+01 05 14.0	$0.28 \times 0.27$	0.0306	-21.67	1	...	$N/A$	...
Akn 120	05 16 11.4	-00 08 59.4	$1.1 \times 0.8$	0.0323	-22.51	1	...	$8.18 \pm 0.06$	4
MCG +08-11-011	05 54 53.5	+46 26 22.0	$2.1 \times 1.5$	0.0205	-20.83	1.5	2	$N/A$	...
Mrk 79	07 42 32.8	+49 48 34.8	$1.2 \times 1.2$	0.0222	-21.35	1.2	2	$7.72 \pm 0.12$	4
Mrk 110	09 25 12.9	+52 17 10.5	$0.67 \times 0.42$	0.0353	-21.26	1.0	2	$7.40 \pm 0.11$	4
NGC 3227	10 23 30.6	+19 51 54.0	$5.4 \times 3.6$	0.0039	-20.03	1.5	2	$6.88 \pm 0.10$	5
NGC 3516	11 06 47.5	+72 34 07.0	$1.7 \times 1.3$	0.0082	-21.07	1.5	2	$7.50 \pm 0.05$	5
Mrk 744	11 39 42.5	+31 54 33.0	$2.2 \times 1.3$	0.0100	-20.16	1.8	2	$N/A$	...
NGC 4051	12 03 09.6	+44 31 52.8	$5.2 \times 3.9$	0.0024	-17.89	1.5	1	$6.24 \pm 0.13$	5
NGC 4151	12 10 32.6	+39 24 20.6	$6.3 \times 4.5$	0.0033	-19.64	1.5	2	$7.66 \pm 0.05$	6
NGC 4593	12 39 39.4	-05 20 39.4	$3.9 \times 2.9$	0.0090	-19.70	1	...	$6.73 \pm 0.66$	4
NGC 5548	14 17 59.5	+25 08 12.4	$1.4 \times 1.3$	0.0172	-21.33	1.5	2	$7.82 \pm 0.02$	7
Mrk 817	14 36 22.1	+58 47 39.4	$0.6 \times 0.6$	0.0315	-22.59	1.5	2	$7.64 \pm 0.11$	5
Mrk 509	20 44 09.7	-10 43 24.5	$0.5 \times 0.5$	0.0344	-23.45	1.2	2	$8.16 \pm 0.04$	4
NGC 7469	23 03 15.6	+08 52 26.4	$1.5 \times 1.1$	0.0163	-21.91	1.2	2	$7.09 \pm 0.05$	4

REFERENCES. — (1) Osterbrock & Martel (1993); (2) Véron-Cetty & Véron (2010); (3) Grier et al. (2012b); (4) Peterson et al. (2004); (5) Denney et al. (2010); (6) Bentz et al. (2006a); (7) Bentz et al. (2007).

<sup>a</sup> Major and minor diameters taken from the NED.

<sup>b</sup> V-band absolute magnitude reported by Véron-Cetty & Véron (2001).

TABLE 2  
SUMMARY OF MONITORING PARAMETERS

Object	Band	Observing period	$n_{\text{obs}}$ <sup>a</sup>	$t_{\text{int,obs}}$ <sup>b</sup>
Mrk 335	<i>V</i>	2003.01.08—2006.01.18	41	15.0
	<i>K</i>	2003.01.08—2006.01.18	40	15.0
Mrk 590	<i>V</i>	2003.01.03—2007.08.08	92	6.5
	<i>K</i>	2003.01.03—2007.08.08	94	6.0
IRAS 03450+0055	<i>V</i>	2002.01.16—2007.08.19	88	9.8
	<i>K</i>	2002.01.16—2007.08.19	86	9.8
Akn 120	<i>V</i>	2001.11.24—2007.08.07	67	13.5
	<i>K</i>	2001.11.24—2007.08.07	69	13.5
MCG +08–11–011	<i>V</i>	2001.01.26—2007.08.19	178	4.0
	<i>K</i>	2001.01.26—2007.08.19	187	4.0
Mrk 79	<i>V</i>	2003.09.08—2006.05.21	47	10.0
	<i>K</i>	2003.09.08—2006.05.11	47	10.0
Mrk 110	<i>V</i>	2003.02.06—2006.05.26	49	15.8
	<i>K</i>	2003.02.06—2006.05.26	50	15.0
NGC 3227	<i>V</i>	2001.11.13—2007.07.01	123	6.0
	<i>K</i>	2001.11.13—2007.07.01	132	6.0
NGC 3516	<i>V</i>	2005.01.16—2007.06.26	35	14.0
	<i>K</i>	2005.01.16—2007.07.02	38	13.1
Mrk 744	<i>V</i>	2002.04.26—2006.05.25	90	7.0
	<i>K</i>	2002.04.26—2006.05.25	94	7.9
NGC 4051	<i>V</i>	2001.03.15—2007.07.30	158	7.0
	<i>K</i>	2001.03.15—2007.07.30	181	6.0
NGC 4151	<i>V</i>	2001.01.06—2007.08.07	234	4.9
	<i>K</i>	2001.01.06—2007.08.07	239	4.9
NGC 4593	<i>V</i>	2005.01.21—2007.07.09	35	13.0
	<i>K</i>	2005.01.21—2007.07.27	37	13.4
NGC 5548	<i>V</i>	2001.03.24—2007.08.20	302	3.0
	<i>K</i>	2001.03.24—2007.08.20	311	3.0
Mrk 817	<i>V</i>	2003.09.04—2006.05.17	38	16.0
	<i>K</i>	2003.09.04—2006.05.17	40	16.0
Mrk 509	<i>V</i>	2003.04.29—2006.05.21	45	13.1
	<i>K</i>	2003.04.29—2006.05.21	49	13.5
NGC 7469	<i>V</i>	2001.06.15—2008.12.08	296	4.0
	<i>K</i>	2001.06.12—2008.12.08	315	4.1

<sup>a</sup> Number of observations.

<sup>b</sup> Median monitoring interval, excluding lengthy observation gaps caused by solar conjunction and occasional facility maintenance.

TABLE 3  
MAGNITUDES OF REFERENCE STARS

Object	Reference star	R.A. (J2000)	Decl. (J2000)	$m_V$ (mag)	$m_K$ (mag)
Mrk 335	A	00 07 04.9	+20 09 53.5	$12.859 \pm 0.004$	$11.348 \pm 0.014$
	B	00 05 51.5	+20 12 33.1	$13.443 \pm 0.004$	$11.354 \pm 0.012$
Mrk 590	A1 <sup>a</sup>	02 14 36.0	-00 39 11.0	$14.128 \pm 0.007$	$13.474 \pm 0.010$
	A2 <sup>a</sup>	02 14 32.2	-00 37 44.4	$12.899 \pm 0.005$	$11.427 \pm 0.006$
	B	02 14 35.1	-00 50 35.6	$14.092 \pm 0.004$	$12.726 \pm 0.005$
IRAS 03450+0055	A	03 47 17.7	+01 06 33.9	$12.865 \pm 0.004$	$11.063 \pm 0.003$
	B	03 47 43.5	+01 00 09.2	$13.208 \pm 0.005$	$11.406 \pm 0.003$
Akn 120	A	05 15 47.9	-00 07 26.3	$13.947 \pm 0.004$	$11.138 \pm 0.006$
	B	05 16 15.1	-00 11 45.2	$11.880 \pm 0.005$	$10.342 \pm 0.005$
MCG +08-11-011	A	05 55 07.6	+46 28 50.8	$13.752 \pm 0.002$	$11.041 \pm 0.004$
	B	05 54 47.8	+46 23 05.0	$12.520 \pm 0.002$	$10.680 \pm 0.004$
Mrk 79	A	07 42 08.2	+49 45 08.1	$13.402 \pm 0.005$	$11.122 \pm 0.004$
	B	07 42 52.2	+49 52 37.4	$12.465 \pm 0.004$	$10.866 \pm 0.004$
Mrk 110	A	09 24 57.1	+52 13 25.6	$14.151 \pm 0.007$	$12.540 \pm 0.006$
	B	09 26 45.9	+52 19 38.5	$14.422 \pm 0.006$	$12.893 \pm 0.006$
NGC 3227	A	10 23 13.5	+19 56 24.6	$12.775 \pm 0.002$	$11.098 \pm 0.003$
	B	10 24 02.9	+19 46 30.0	$11.963 \pm 0.003$	$10.467 \pm 0.003$
NGC 3516	A	11 03 46.0	+72 25 36.9	$12.846 \pm 0.008$	$10.906 \pm 0.009$
	B	11 08 33.2	+72 37 57.1	$13.429 \pm 0.009$	$11.532 \pm 0.011$
Mrk 744	A	11 38 59.2	+31 59 26.4	$14.259 \pm 0.007$	$12.617 \pm 0.006$
	B	11 39 58.2	+31 50 04.3	$14.114 \pm 0.006$	$12.619 \pm 0.006$
NGC 4051	A	12 04 13.1	+44 55 01.5	$12.643 \pm 0.003$	$9.976 \pm 0.005$
	B	12 03 30.1	+44 16 45.5	$13.881 \pm 0.003$	$10.273 \pm 0.005$
NGC 4151	A	12 11 37.2	+39 29 59.7	$11.926 \pm 0.002$	$10.513 \pm 0.003$
	B	12 09 47.3	+39 15 02.8	$11.913 \pm 0.002$	$10.592 \pm 0.003$
NGC 4593	A	12 40 08.0	-05 22 35.7	$12.711 \pm 0.003$	$10.987 \pm 0.010$
	B	12 39 16.6	-05 27 12.3	$13.109 \pm 0.004$	$11.429 \pm 0.007$
NGC 5548	A	14 17 58.8	+25 05 33.3	$13.789 \pm 0.002$	$12.193 \pm 0.003$
	B	14 17 14.7	+25 19 21.7	$13.134 \pm 0.002$	$11.529 \pm 0.003$
Mrk 817	A	14 36 00.7	+58 39 15.4	$13.437 \pm 0.006$	$11.435 \pm 0.011$
	B	14 36 26.8	+58 57 13.8	$12.807 \pm 0.006$	$11.541 \pm 0.011$
Mrk 509	A	20 44 48.5	-10 58 00.8	$13.402 \pm 0.005$	$10.132 \pm 0.010$
	B	20 43 39.1	-10 43 27.7	$12.646 \pm 0.004$	$10.192 \pm 0.011$
NGC 7469	B <sup>b</sup>	23 02 23.3	+09 06 40.4	$12.999 \pm 0.001$	$10.693 \pm 0.004$

<sup>a</sup> The reference star was changed from A1 to A2 on July 12, 2004.

<sup>b</sup> The reference star A for NGC 7469 was not used for photometry.

TABLE 4  
LIGHT CURVE DATA

Object	Band	Observation Date (MJD)	Flux (mJy)	Flux Error (mJy)
Mrk 335	<i>V</i>	52647.31	7.69	0.08
Mrk 335	<i>V</i>	52797.60	6.87	0.14
...	...	...	...	...
Mrk 335	<i>K</i>	52647.31	36.03	0.30
Mrk 335	<i>K</i>	52797.60	33.41	0.28
...	...	...	...	...

NOTE. — Correction for the Galactic extinction has not been applied to the light curves, and the fluxes from the host galaxy and narrow emission lines have not been subtracted. The complete data of this table is available in a machine-readable form in the online journal. A portion is shown here for guidance.



TABLE 5  
CONTRIBUTION OF HOST-GALAXY FLUX AND NARROW EMISSION LINES TO THE  
OBSERVED FLUX

Object	Band	$f_{\text{host}}^{\text{a}}$ (mJy)	Ref.	$f_{\text{NL}}^{\text{b}}$ (mJy)	Ref.	total (mJy)
Mrk 335	V	$2.03 \pm 0.10$	1	0.20	1	$2.23 \pm 0.10$
	K	$5.02 \pm 0.25$	1	...		$5.02 \pm 0.25$
Mrk 590	V	$4.24 \pm 0.06$	2	0.16	2	$4.39 \pm 0.06$
	K	$22.18 \pm 0.13$	1	...		$22.18 \pm 0.13$
IRAS 03450+0055	V	$0.65 \pm 0.09$	4	0.17	1	$0.82 \pm 0.09$
	K	$5.15 \pm 0.33$	4	...		$5.15 \pm 0.33$
Akn 120	V	$3.09 \pm 0.07$	4	0.18	1	$3.27 \pm 0.07$
	K	$20.02 \pm 0.77$	4	...		$20.02 \pm 0.77$
MCG +08-11-011	V	$2.24 \pm 0.17$	4	0.44	1	$2.68 \pm 0.18$
	K	$16.78 \pm 1.00$	4	...		$16.78 \pm 1.00$
Mrk 79	V	$2.39 \pm 0.10$	1	0.24	1	$2.63 \pm 0.11$
	K	$10.30 \pm 1.11$	1	...		$10.30 \pm 1.11$
Mrk 110	V	$0.71 \pm 0.09$	2	0.10	2	$0.81 \pm 0.09$
	K	$4.14 \pm 0.71$	1	...		$4.14 \pm 0.71$
NGC 3227	V	$8.03 \pm 0.30$	2	0.51	2	$8.53 \pm 0.30$
	K	$57.86 \pm 1.66$	3	...		$57.86 \pm 1.66$
NGC 3516	V	$14.12 \pm 0.25$	2	0.21	2	$14.34 \pm 0.25$
	K	$68.81 \pm 0.53$	1	...		$68.81 \pm 0.53$
Mrk 744	V	$3.25 \pm 0.02$	1	0.08	1	$3.33 \pm 0.02$
	K	$21.83 \pm 0.11$	1	...		$21.83 \pm 0.11$
NGC 4051	V	$7.74 \pm 0.36$	2	0.29	2	$8.03 \pm 0.37$
	K	$39.05 \pm 1.36$	3	...		$39.05 \pm 1.36$
NGC 4151	V	$17.17 \pm 0.83$	2	9.13	2	$26.30 \pm 1.23$
	K	$44.22 \pm 3.83$	5	...		$44.22 \pm 3.83$
NGC 4593	V	$6.73 \pm 0.08$	2	0.16	2	$6.89 \pm 0.08$
	K	$34.40 \pm 0.22$	1	...		$34.40 \pm 0.22$
NGC 5548	V	$3.97 \pm 0.04$	2	0.37	2	$4.34 \pm 0.05$
	K	$15.21 \pm 0.33$	3	...		$15.21 \pm 0.33$
Mrk 817	V	$1.26 \pm 0.04$	2	0.27	2	$1.53 \pm 0.05$
	K	$6.55 \pm 0.72$	1	...		$6.55 \pm 0.72$
Mrk 509	V	$2.96 \pm 0.19$	1	0.82	1	$3.78 \pm 0.21$
	K	$11.57 \pm 0.64$	1	...		$11.57 \pm 0.64$
NGC 7469	V	$8.61 \pm 0.31$	3	0.69	1	$9.30 \pm 0.31$
	K	$59.64 \pm 1.65$	3	...		$59.64 \pm 1.65$

REFERENCES. — (1) This study; (2) Sakata et al. (2010); (3) Suganuma et al. (2006); (4) Tomita et al. (2006); (5) Minezaki et al. (2004).

NOTE. — Correction for the Galactic extinction has not been applied.

<sup>a</sup> The host-galaxy flux within the photometric aperture of  $\phi = 8''.3$ .

<sup>b</sup> The contribution of [O III] $\lambda$ 4959 and  $\lambda$ 5007 emission lines to the V-band flux.

TABLE 6  
PARAMETERS OF POWER-LAW  
FITTING OF THE  $V$ -BAND  
STRUCTURE FUNCTION

Object	$\alpha$	$\beta$
Mrk 335	0.0049	0.88
Mrk 590	0.0003	1.02
IRAS 03450+0055	0.0005	1.38
Akn 120	0.0385	0.84
MCG +08-11-011	0.0111	0.94
Mrk 79	0.0015	1.34
Mrk 110	0.0024	1.21
NGC 3227	0.0523	0.67
NGC 3516	0.0026	1.83
Mrk 744	0.0007	1.03
NGC 4051	0.0343	0.78
NGC 4151	0.7197	0.92
NGC 4593	0.0012	1.44
NGC 5548	0.0018	1.46
Mrk 817	0.0006	1.39
Mrk 509	0.0296	1.02
NGC 7469	0.0334	0.87

TABLE 7  
LAG TIME AND *V*-BAND ABSOLUTE MAGNITUDE FOR THE TARGETS

Object	Section <sup>a</sup>	MJD	$M_V$ (mag)	$\Delta t_K(\text{CCF})^b$ (days)	$\Delta t_K(\text{CCF})^c$ (days)	$\Delta t_K(\text{JAVELIN})^b$ (days)	$\Delta t_K(\text{JAVELIN})^c$ (days)
Mrk 335	1	52647.3—53753.3	$-20.63 \pm 0.02$	$142.2^{+16.8}_{-16.6}$	$132.1^{+18.0}_{-13.6}$	$167.1^{+5.4}_{-5.9}$	$165.8^{+6.0}_{-7.4}$
	WA	...	$-20.63 \pm 0.02$	$142.2 \pm 16.7$	$132.1 \pm 15.8$	$167.1 \pm 5.6$	$165.8 \pm 6.7$
Mrk 590	1	52842.6—53429.2	$-18.69 \pm 0.08$	$37.2^{+3.1}_{-2.3}$	$35.9^{+2.7}_{-2.7}$	$33.8^{+4.2}_{-4.2}$	$32.2^{+4.0}_{-4.0}$
	WA	...	$-18.69 \pm 0.08$	$37.2 \pm 2.7$	$35.9 \pm 2.7$	$33.8 \pm 4.2$	$32.2 \pm 4.0$
IRAS 03450+0055	1	52290.4—52709.3	$-21.48 \pm 0.02$	$95.5^{+7.3}_{-4.4}$	$93.1^{+6.0}_{-4.8}$	$156.3^{+10.7}_{-8.4}$	$136.8^{+14.9}_{-13.5}$
	2	52574.5—53453.2	$-21.30 \pm 0.03$	$167.3^{+10.2}_{-11.7}$	$146.0^{+14.0}_{-18.2}$	$166.3^{+6.8}_{-6.8}$	$165.3^{+8.0}_{-9.4}$
	3	53578.6—54013.4	$-21.53 \pm 0.02$	$88.5^{+16.4}_{-8.8}$	$70.3^{+10.7}_{-8.1}$	$97.5^{+24.3}_{-15.9}$	$95.0^{+27.9}_{-22.4}$
	WA	...	$-21.41 \pm 0.02$	$108.2 \pm 4.8$	$92.0 \pm 4.5$	$158.3 \pm 5.4$	$152.5 \pm 7.1$
Akn 120	1	53594.6—54319.6	$-22.23 \pm 0.02$	$138.8^{+22.1}_{-12.8}$	$127.6^{+17.2}_{-13.1}$	$140.9^{+18.5}_{-15.9}$	$129.7^{+19.3}_{-16.8}$
	WA	...	$-22.23 \pm 0.02$	$138.8 \pm 17.5$	$127.6 \pm 15.2$	$140.9 \pm 17.2$	$129.7 \pm 18.0$
MCG +08–11–011	1	52158.6—53124.3	$-20.62 \pm 0.04$	$111.1^{+20.0}_{-21.3}$	$114.9^{+18.3}_{-22.0}$	$63.9^{+1.7}_{-1.3}$	$69.3^{+2.5}_{-2.1}$
	2	53593.6—54224.3	$-19.27 \pm 0.16$	$83.4^{+14.1}_{-23.2}$	$67.6^{+11.5}_{-21.3}$	$127.1^{+3.6}_{-3.6}$	$72.1^{+2.7}_{-6.5}$
	WA	...	$-20.25 \pm 0.06$	$95.8 \pm 13.8$	$86.4 \pm 12.7$	$73.5 \pm 1.4$	$69.9 \pm 2.1$
Mrk 79	1	52890.6—53150.3	$-20.06 \pm 0.04$	$52.9^{+8.8}_{-6.2}$	$50.7^{+5.4}_{-5.0}$	$60.2^{+5.9}_{-6.0}$	$57.9^{+6.3}_{-7.4}$
	2	53369.3—53876.3	$-19.78 \pm 0.05$	$80.3^{+3.6}_{-4.6}$	$72.8^{+3.1}_{-3.0}$	$78.6^{+8.9}_{-9.5}$	$80.4^{+5.3}_{-5.5}$
	WA	...	$-19.98 \pm 0.04$	$74.0 \pm 3.6$	$67.0 \pm 2.6$	$65.6 \pm 5.0$	$71.8 \pm 4.2$
Mrk 110	1	52676.3—53163.3	$-19.90 \pm 0.09$	$87.6^{+7.6}_{-8.5}$	$80.2^{+7.1}_{-8.5}$	$113.1^{+8.8}_{-8.6}$	$103.2^{+10.9}_{-13.5}$
	2	53291.6—53881.3	$-20.94 \pm 0.03$	$93.8^{+8.8}_{-10.5}$	$89.3^{+7.9}_{-9.2}$	$124.1^{+7.1}_{-7.1}$	$109.4^{+12.3}_{-8.8}$
	WA	...	$-20.63 \pm 0.04$	$90.3 \pm 6.1$	$84.3 \pm 5.8$	$119.7 \pm 5.5$	$106.8 \pm 8.0$
NGC 3227	1	52226.6—52423.3	$-16.88 \pm 0.08$	$18.9^{+4.3}_{-4.8}$	$18.2^{+4.4}_{-4.9}$	$26.9^{+3.9}_{-3.8}$	$25.3^{+4.3}_{-3.8}$
	2	52935.6—53176.3	$-16.95 \pm 0.07$	$17.4^{+3.6}_{-4.4}$	$15.6^{+3.2}_{-3.7}$	$15.8^{+2.4}_{-2.0}$	$14.9^{+2.2}_{-1.9}$
	3	53350.5—53485.4	$-17.25 \pm 0.05$	$19.7^{+1.3}_{-1.5}$	$18.9^{+1.4}_{-1.3}$	$16.9^{+10.8}_{-2.3}$	$14.0^{+3.2}_{-2.3}$
	4	53664.6—53790.4	$-17.07 \pm 0.06$	$10.7^{+1.7}_{-1.6}$	$10.0^{+1.9}_{-1.7}$	$10.2^{+2.8}_{-2.5}$	$9.4^{+3.0}_{-2.6}$
	5	53723.6—53904.3	$-16.96 \pm 0.07$	$15.4^{+1.7}_{-1.8}$	$14.8^{+1.7}_{-1.9}$	$18.7^{+5.6}_{-3.0}$	$19.6^{+4.5}_{-3.6}$
	6	54181.4—54282.3	$-16.99 \pm 0.06$	$12.9^{+1.0}_{-0.8}$	$11.6^{+0.8}_{-0.8}$	$14.1^{+0.8}_{-0.8}$	$13.2^{+0.9}_{-0.8}$
	WA	...	$-17.06 \pm 0.06$	$14.5 \pm 0.6$	$13.3 \pm 0.6$	$14.6 \pm 0.7$	$13.8 \pm 0.7$
NGC 3516	1	53386.4—53920.3	$-18.14 \pm 0.09$	$52.9^{+7.0}_{-12.0}$	$47.3^{+8.7}_{-11.1}$	$73.1^{+3.9}_{-4.0}$	$71.5^{+5.4}_{-6.2}$
	WA	...	$-18.14 \pm 0.09$	$52.9 \pm 9.5$	$47.3 \pm 9.9$	$73.1 \pm 4.0$	$71.5 \pm 5.8$
Mrk 744	1	52994.5—53208.3	$-16.18 \pm 0.06$	$16.2^{+2.4}_{-2.7}$	$15.6^{+2.3}_{-2.2}$	$17.0^{+3.1}_{-3.1}$	$16.6^{+3.1}_{-3.2}$
	2	53336.6—53550.3	$-16.04 \pm 0.08$	$28.5^{+3.7}_{-3.5}$	$28.1^{+3.9}_{-3.2}$	$23.0^{+3.3}_{-2.8}$	$22.6^{+3.3}_{-2.9}$
	WA	...	$-16.12 \pm 0.05$	$20.4 \pm 2.1$	$19.2 \pm 1.9$	$20.0 \pm 2.2$	$19.7 \pm 2.2$
NGC 4051	1	52286.6—52488.3	$-15.74 \pm 0.10$	$12.5^{+1.0}_{-1.1}$	$11.9^{+1.0}_{-1.2}$	$15.9^{+1.7}_{-1.7}$	$14.5^{+0.9}_{-0.8}$
	2	52599.6—52832.3	$-15.78 \pm 0.09$	$23.4^{+2.4}_{-2.4}$	$22.9^{+2.3}_{-2.3}$	$24.8^{+1.1}_{-1.0}$	$25.0^{+1.1}_{-1.2}$
	3	53341.6—53577.3	$-15.69 \pm 0.10$	$20.2^{+4.6}_{-5.5}$	$18.3^{+4.6}_{-4.4}$	$24.0^{+12.9}_{-12.9}$	$22.9^{+13.4}_{-13.4}$
	4	53684.6—53937.3	$-15.73 \pm 0.10$	$16.3^{+1.3}_{-1.2}$	$15.5^{+1.2}_{-1.1}$	$11.9^{+1.2}_{-0.9}$	$13.4^{+1.0}_{-1.4}$
	5	54202.5—54252.4	$-15.77 \pm 0.09$	$11.0^{+0.9}_{-1.2}$	$10.7^{+1.4}_{-1.2}$	$9.9^{+2.5}_{-1.9}$	$9.6^{+2.3}_{-2.1}$
	6	54221.5—54278.3	$-15.75 \pm 0.09$	$12.4^{+1.5}_{-1.1}$	$12.3^{+1.2}_{-1.1}$	$13.0^{+2.4}_{-2.4}$	$12.7^{+2.6}_{-2.6}$
	7	54252.4—54311.3	$-15.73 \pm 0.10$	$16.7^{+0.8}_{-0.7}$	$16.2^{+0.7}_{-0.8}$	$15.2^{+2.1}_{-2.0}$	$14.6^{+1.9}_{-2.1}$
NGC 4151	WA	...	$-15.75 \pm 0.09$	$14.7 \pm 0.5$	$14.3 \pm 0.4$	$16.5 \pm 0.6$	$15.8 \pm 0.5$
	1	51915.6—52127.3	$-17.78 \pm 0.13$	$59.6^{+1.1}_{-1.3}$	$53.9^{+1.7}_{-2.4}$	$59.7^{+1.5}_{-1.4}$	$56.6^{+1.1}_{-1.2}$
	2	52265.5—52646.6	$-18.59 \pm 0.07$	$70.3^{+14.0}_{-13.0}$	$64.7^{+19.6}_{-16.3}$	$68.8^{+2.0}_{-1.3}$	$70.0^{+4.4}_{-2.7}$
	3	52610.6—53010.5	$-18.95 \pm 0.05$	$59.1^{+2.0}_{-2.4}$	$56.4^{+2.1}_{-3.1}$	$60.1^{+1.8}_{-1.5}$	$58.1^{+1.8}_{-1.6}$
	4	53039.4—53356.5	$-18.19 \pm 0.10$	$65.1^{+2.9}_{-3.0}$	$62.9^{+2.8}_{-3.0}$	$66.2^{+8.1}_{-2.9}$	$65.3^{+3.1}_{-2.8}$
	5	53148.4—53490.3	$-18.09 \pm 0.11$	$50.4^{+6.9}_{-12.1}$	$45.1^{+7.1}_{-12.0}$	$81.2^{+3.1}_{-2.2}$	$82.7^{+4.2}_{-3.0}$
	6	53436.4—53687.6	$-17.94 \pm 0.13$	$41.2^{+5.1}_{-3.8}$	$37.7^{+4.8}_{-3.3}$	$42.0^{+0.4}_{-0.8}$	$41.9^{+0.5}_{-1.3}$
NGC 4593	7	53687.6—53864.4	$-18.21 \pm 0.09$	$33.1^{+2.3}_{-2.3}$	$31.8^{+1.9}_{-2.7}$	$38.7^{+2.6}_{-2.6}$	$36.0^{+0.5}_{-0.4}$
	8	53753.4—53921.3	$-18.02 \pm 0.10$	$38.5^{+1.3}_{-1.2}$	$36.8^{+1.1}_{-1.2}$	$41.7^{+1.9}_{-1.0}$	$40.2^{+0.6}_{-0.7}$
	WA	...	$-18.14 \pm 0.09$	$49.7 \pm 0.7$	$43.1 \pm 0.8$	$48.3 \pm 0.5$	$40.9 \pm 0.3$
	1	53391.5—53930.3	$-17.93 \pm 0.04$	$43.5^{+1.9}_{-1.6}$	$44.0^{+2.1}_{-1.8}$	$41.6^{+0.9}_{-0.8}$	$42.1^{+0.8}_{-1.1}$
	WA	...	$-17.93 \pm 0.04$	$43.5 \pm 1.8$	$44.0 \pm 2.0$	$41.6 \pm 0.9$	$42.1 \pm 0.9$
	1	51992.5—52389.5	$-19.33 \pm 0.03$	$62.9^{+1.2}_{-1.5}$	$57.4^{+1.4}_{-1.4}$	$63.8^{+0.8}_{-0.9}$	$56.8^{+1.7}_{-2.6}$
	2	52308.6—52797.4	$-18.84 \pm 0.05$	$67.7^{+5.4}_{-5.7}$	$61.5^{+4.7}_{-5.7}$	$59.9^{+0.4}_{-0.4}$	$55.3^{+1.1}_{-0.4}$
NGC 5548	3	52638.6—52999.6	$-19.13 \pm 0.04$	$62.5^{+3.2}_{-4.1}$	$59.3^{+3.1}_{-3.8}$	$79.3^{+1.7}_{-1.9}$	$76.3^{+1.8}_{-2.0}$
	4	53168.4—53437.5	$-18.57 \pm 0.05$	$49.1^{+4.8}_{-5.2}$	$45.7^{+4.3}_{-4.8}$	$45.5^{+5.0}_{-5.0}$	$44.1^{+5.9}_{-5.9}$
	5	53350.6—53527.4	$-18.56 \pm 0.05$	$41.7^{+1.4}_{-1.4}$	$40.5^{+1.5}_{-1.4}$	$42.8^{+3.1}_{-3.1}$	$41.7^{+2.9}_{-3.1}$
	6	54181.6—54332.3	$-18.41 \pm 0.05$	$57.0^{+1.0}_{-0.9}$	$55.1^{+0.8}_{-0.8}$	$57.4^{+1.9}_{-1.9}$	$62.7^{+0.4}_{-0.3}$
	WA	...	$-18.77 \pm 0.02$	$55.2 \pm 0.7$	$53.0 \pm 0.6$	$60.9 \pm 0.3$	$61.3 \pm 0.3$
	1	53353.6—53872.5	$-20.86 \pm 0.02$	$89.8^{+9.6}_{-7.0}$	$83.5^{+8.6}_{-6.5}$	$93.0^{+9.4}_{-8.5}$	$89.8^{+8.8}_{-8.4}$
	WA	...	$-20.86 \pm 0.02$	$89.8 \pm 8.3$	$83.5 \pm 7.6$	$93.0 \pm 8.9$	$89.8 \pm 8.6$
Mrk 509	1	52758.6—53867.6	$-22.13 \pm 0.03$	$149.2^{+9.8}_{-8.6}$	$133.4^{+9.5}_{-8.0}$	$120.7^{+2.6}_{-1.0}$	$120.3^{+1.3}_{-1.0}$
	WA	...	$-22.13 \pm 0.03$	$149.2 \pm 9.2$	$133.4 \pm 8.8$	$120.7 \pm 1.8$	$120.3 \pm 1.1$

TABLE 7  
(CONTINUED)

Object	Section <sup>a</sup>	MJD	$M_V$ (mag)	$\Delta t_K(\text{CCF})^b$ (days)	$\Delta t_K(\text{CCF})^c$ (days)	$\Delta t_K(\text{JAVELIN})^b$ (days)	$\Delta t_K(\text{JAVELIN})^c$ (days)
NGC 7469	1	52072.5—52647.2	$-19.85 \pm 0.06$	$97.5^{+5.2}_{-4.9}$	$98.7^{+5.8}_{-5.7}$	$88.4^{+1.4}_{-1.5}$	$94.1^{+0.2}_{-0.5}$
	2	52787.6—53369.3	$-19.68 \pm 0.07$	$37.0^{+2.1}_{-2.8}$	$37.9^{+3.1}_{-3.1}$	$106.8^{+1.0}_{-1.1}$	$106.4^{+0.9}_{-1.2}$
	3	53508.6—54017.3	$-19.84 \pm 0.06$	$103.9^{+4.2}_{-4.0}$	$92.5^{+6.1}_{-4.0}$	<sup>d</sup> $125.4^{+2.7}_{-2.7}$	$122.9^{+0.2}_{-0.2}$
	4	54233.6—54808.3	$-19.75 \pm 0.07$	$33.6^{+1.5}_{-2.6}$	$32.4^{+2.1}_{-3.4}$	$74.4^{+0.1}_{-1.5}$	$74.43^{+0.05}_{-0.06}$
	WA	...	$-19.79 \pm 0.06$	$48.3 \pm 1.4$	$48.6 \pm 1.8$	$88.0 \pm 0.6$	$78.12 \pm 0.05$

NOTE. — The lag times in the observed frame were presented.

<sup>a</sup> The row of the notation WA presents the weighted averaged  $V$ -band absolute magnitude and the weighted averaged lag time for the individual targets.

<sup>b</sup> Assuming  $\alpha_\nu = 0$  for the subtraction of the accretion-disk component in the  $K$ -band flux.

<sup>c</sup> Assuming  $\alpha_\nu = +1/3$  for the subtraction of the accretion-disk component in the  $K$ -band flux.

<sup>d</sup> The middle point of the 16 and 84 %-ile lag times of the likelihood distribution was adopted because ambiguous multiple peaks appeared.

TABLE 8  
RESULTS OF LINEAR REGRESSION OF DUST LAG-LUMINOSITY CORRELATION

Lag Method	N <sup>a</sup> (km s <sup>-1</sup> )	V <sub>pec</sub>	$\sigma_{\text{add}}^c$	$a^c$	reduced $\chi^2$ <sup>c</sup>	$\sigma_{\text{add}}^d$	$a^d$	reduced $\chi^2$ <sup>d</sup>
CCF	49	—	—	$-2.052 \pm 0.004$	22.7	—	$-2.074 \pm 0.004$	21.2
	17	—	—	$-2.080 \pm 0.005$	37.2	—	$-2.093 \pm 0.005$	38.0
	17	200	—	$-2.141 \pm 0.008$	14.4	—	$-2.166 \pm 0.008$	15.9
	17	300	—	$-2.157 \pm 0.010$	9.4	—	$-2.187 \pm 0.010$	10.5
	17	—	0.140	$-2.113 \pm 0.035$	1.0 <sup>b</sup>	0.144	$-2.146 \pm 0.036$	1.0 <sup>b</sup>
	17	200	0.136	$-2.117 \pm 0.035$	1.0 <sup>b</sup>	0.140	$-2.150 \pm 0.036$	1.0 <sup>b</sup>
JAVELIN	17	300	0.131	$-2.122 \pm 0.035$	1.0 <sup>b</sup>	0.135	$-2.154 \pm 0.036$	1.0 <sup>b</sup>
	49	—	—	$-2.051 \pm 0.003$	66.5	—	$-2.057 \pm 0.003$	72.5
	17	—	—	$-2.051 \pm 0.003$	131.8	—	$-2.072 \pm 0.003$	157.0
	17	200	—	$-2.127 \pm 0.006$	49.9	—	$-2.157 \pm 0.006$	48.5
	17	300	—	$-2.131 \pm 0.008$	29.9	—	$-2.156 \pm 0.008$	28.2
	17	—	0.162	$-2.078 \pm 0.040$	1.0 <sup>b</sup>	0.162	$-2.096 \pm 0.040$	1.0 <sup>b</sup>
	17	200	0.159	$-2.081 \pm 0.040$	1.0 <sup>b</sup>	0.159	$-2.098 \pm 0.040$	1.0 <sup>b</sup>
	17	300	0.156	$-2.084 \pm 0.040$	1.0 <sup>b</sup>	0.156	$-2.100 \pm 0.040$	1.0 <sup>b</sup>

NOTE. — The fitted model is  $\log \Delta t_K = a - 0.2M_V$ .

<sup>a</sup> The number of the data pair for the fitting.  $N = 49$  indicates that all measured lag times and absolute magnitudes were used;  $N = 17$  indicates that the weighted averaged lag times and absolute magnitudes for individual targets were used.

<sup>b</sup>  $\sigma_{\text{add}}$  was added to the error of  $\log \Delta t_K$  by root-sum-square for the reduced  $\chi^2$  to achieve unity.

<sup>c</sup> Assuming  $\alpha_\nu = 0$  for the subtraction of the accretion-disk component in the  $K$ -band flux.

<sup>d</sup> Assuming  $\alpha_\nu = +1/3$  for the subtraction of the accretion-disk component in the  $K$ -band flux.

TABLE 9  
RESULTS OF LINEAR REGRESSION OF RADIUS-LUMINOSITY CORRELATION

Source	$L$ (erg s <sup>-1</sup> )	N <sup>a</sup>	$\alpha$	$\beta^b$	$\sigma_{\text{add}}^c$	Ref.
near-infrared interferometry	$L_V/10^{44}$	9	$-0.72 \pm 0.06$	0.5	0.15	1
	$L_{\text{BAT}}/10^{44}$	6	$-0.63 \pm 0.10$	0.5	0.21	1
dust reverberation <sup>d</sup>	$L_{[\text{OIV}]} / 10^{41}$	7	$-0.94 \pm 0.09$	0.5	0.19	1
	$L_V/10^{44}$	17	$-0.89 \pm 0.04$	0.5	0.14	1
			$-0.92 \pm 0.04$	0.5	0.14	1
			$-0.85 \pm 0.04$	0.5	0.16	1
			$-0.87 \pm 0.04$	0.5	0.16	1
	$L_{\text{BAT}}/10^{44}$	16	$-1.04 \pm 0.04$	0.5	0.16	1
			$-1.07 \pm 0.04$	0.5	0.16	1
			$-1.01 \pm 0.05$	0.5	0.19	1
			$-1.03 \pm 0.05$	0.5	0.19	1
	$L_{[\text{OIV}]} / 10^{41}$	14	$-1.29 \pm 0.06$	0.5	0.21	1
$-1.32 \pm 0.06$			0.5	0.21	1	
$-1.25 \pm 0.07$			0.5	0.25	1	
$-1.26 \pm 0.07$			0.5	0.24	1	
BLR reverberation	$L_V/10^{44}$	34	-1.51	$0.519^{+0.063}_{-0.066}$	—	2
	$L_{\text{BAT}}/10^{44}$	36	$-1.78 \pm 0.04$	0.5	0.25	1
	$L_{[\text{OIV}]} / 10^{41}$	33	$-1.94 \pm 0.07$	0.5	0.36	1
	$L_{[\text{OIV}]} / 10^{41}$	26	$-1.88 \pm 0.10$	$0.58 \pm 0.11$	0.35	3

REFERENCES. — (1) This study; (2) Bentz et al. (2009b); (3) Greene et al. (2010).

NOTE. — The fitted model is  $\log r = \alpha + \beta \log L$ .

<sup>a</sup> The number of the data pair for the fitting.

<sup>b</sup>  $\beta = 0.5$  is assumed for the fitting when that value is presented.

<sup>c</sup>  $\sigma_{\text{add}}$  was added to the error of  $\log r$  by root-sum-square for the reduced  $\chi^2$  to achieve unity.

<sup>d</sup> The lag times  $\Delta t$  were derived by the two different lag-analysis methods assuming the two different  $\alpha_\nu$  values for the subtraction of the accretion-disk component in the  $K$ -band flux. The values of  $\alpha$  and  $\sigma_{\text{add}}$  in four rows for each lag-luminosity correlation were obtained from the lag times of  $\Delta t(\text{CCF}; \alpha_\nu = 0)$ ,  $\Delta t(\text{CCF}; \alpha_\nu = +1/3)$ ,  $\Delta t(\text{JAVELIN}; \alpha_\nu = 0)$ , and  $\Delta t(\text{JAVELIN}; \alpha_\nu = +1/3)$ , respectively.